nature neuroscience

ARTICLES

https://doi.org/10.1038/s41593-022-01104-7

A shared disease-associated oligodendrocyte signature among multiple CNS pathologies

Mor Kenigsbuch[1,2,10], Pierre Bost[2,3,4,5,10], Shahar Halevi[1,2], Yuzhou Chang[6,7], Shuo Chen[7,8], Qin Ma[6], Renana Hajbi[9], Benno Schwikowski[3], Bernd Bodenmiller[5], Hongjun Fu[8], Michal Schwartz[1,11] ✉ and Ido Amit[2,11] ✉

Alzheimer's disease (AD) is a complex neurodegenerative disease, perturbing neuronal and non-neuronal cell populations. In this study, using single-cell transcriptomics, we mapped all non-immune, non-neuronal cell populations in wild-type and AD model (5xFAD) mouse brains. We identified an oligodendrocyte state that increased in association with brain pathology, which we termed disease-associated oligodendrocytes (DOLs). In a murine model of amyloidosis, DOLs appear long after plaque accumulation, and amyloid-beta (Aβ) alone was not sufficient to induce the DOL signature in vitro. DOLs could be identified in a mouse model of tauopathy and in other murine neurodegenerative and autoimmune inflammatory conditions, suggesting a common response to severe pathological conditions. Using quantitative spatial analysis of mouse and postmortem human brain tissues, we found that oligodendrocytes expressing a key DOL marker (SERPINA3N/SERPINA3 accordingly) are present in the cortex in areas of brain damage and are enriched near Aβ plaques. In postmortem human brain tissue, the expression level of this marker correlated with cognitive decline. Altogether, this study uncovers a shared signature of oligodendrocytes in central nervous system pathologies.

Alzheimer's disease (AD) is the most common age-related neurodegenerative disease and form of dementia[1,2]. It is considered one of the main public health challenges in Western countries due to population aging. Pathological hallmarks include accumulation of misfolded protein aggregates of amyloid-beta (Aβ), collectively known as amyloid plaques, neurofibrillary tangles caused by hyper-phosphorylated protein tau[2–4] as well as local brain inflammation[5–8]. Despite intensive research, no disease-modifying therapy has been found, and disease management is complex and inefficient[1,2]. This also applies to other forms of dementia, stressing the need for an in-depth understanding of the cellular and molecular pathways underlying disease onset and progression.

Although AD research has been neuron-centric for decades, studies over the last two decades have highlighted the fate of non-neuronal cells and their potential contribution to disease progression. The introduction of single-cell RNA sequencing (scRNA-seq) techniques further advanced the field by uncovering new pathways and cell types associated with the disease, primarily in microglia and astrocytes[9–11]. Oligodendrocytes, which comprise about 20% of all cells in the brain, are the central nervous system (CNS) myelin-forming cells. In the context of AD and dementia, substantial myelin alterations and breakdown have been observed both in the brain of deceased patients and in mouse models[12–14]. However, despite the vital function of oligodendrocytes in the brain, it is unclear if and how their fate is altered in AD and, if so, whether it is etiology dependent or conserved across pathologies.

Using massively parallel single-cell RNA sequencing (MARS-seq), we discovered an oligodendrocyte cell state arising in the 5xFAD mouse model, which we termed DOLs. By re-analyzing published datasets, we found a similar cell state both in different models of dementia-associated pathology and in autoimmune neuroinflammation, indicating that this state arises in multiple disease states. Using immunohistochemistry and spatial transcriptomics, we found DOL-like cells in areas enriched with Aβ plaques in the 5xFAD brain. DOL-like cells were also found in postmortem temporal cortex of patients with AD but not in non-demented controls. Overall, our study uncovers that oligodendrocyte response to different CNS pathologies is disease etiology independent.

Results

Oligodendrocytes display major transcriptomic alterations in the 5xFAD mouse model. Oligodendrocytes are often viewed as passive bystander cells with limited responsiveness to extrinsic cues. Therefore, we were interested to find out if their molecular landscape is altered under AD-associated conditions relative to other non-neuronal cells, which are considered more dynamic. To this end, we performed MARS-seq 2.0 (refs. [15,16]) of non-immune, non-neuronal ($CD45^-$) cells, isolated from whole brains of wild-type (WT) and 5xFAD mice (6–8 months: $n=4$ 5xFAD, 4 WT; 10–11 months: $n=3$ 5xFAD, 4 WT; 15 months: $n=2$ 5xFAD, 1 WT)—a murine model of amyloidosis carrying five familial AD mutations and featuring a progressive appearance of Aβ plaques[17] (all the mice characteristics used in this study are described in

[1]Department of Neurobiology, Weizmann Institute of Science, Rehovot, Israel. [2]Department of Immunology, Weizmann Institute of Science, Rehovot, Israel. [3]Systems Biology Group, Center for Bioinformatics, Biostatistics and Integrative Biology, Institut Pasteur CNRS, Paris, France. [4]Sorbonne Université, Complexité du vivant, Paris, France. [5]University of Zurich, Zurich, Switzerland. [6]Department of Biomedical Informatics, College of Medicine, Ohio State University, Columbus, OH, USA. [7]Biomedical Sciences Graduate Program, Ohio State University, Columbus, OH, USA. [8]Department of Neuroscience, College of Medicine, Ohio State University, Columbus, OH, USA. [9]Department of Molecular Cell Biology, Weizmann Institute of Science, Rehovot, Israel. [10]These authors contributed equally: Mor Kenigsbuch, Pierre Bost. [11]These authors jointly supervised this work: Michal Schwartz, Ido Amit. ✉e-mail: michal.schwartz@weizmann.ac.il; ido.amit@weizmann.ac.il

Supplementary Table 1). After strict quality controls (Extended Data Fig. 1a–c), 10,690 cells were analyzed, and no significant difference in cell library quality was observed between WT and 5xFAD mice (Extended Data Fig. 1d). Cells were clustered based on their expression profile using the Pagoda2 (ref. [18]) pipeline, and 17 clusters were detected and annotated based on established cell-type-specific marker genes (Fig. 1a,b and Extended Data Fig. 1e). The major populations that were identified were mature myelinating oligodendrocytes (*Plp1*, *Mbp* and *Mog*), astrocytes (*Slc1a2* and *Slc1a3*), pericytes (*Myl9*, *Vtn* and *Rgs5*), endothelial cells (*Ly6a* and *Ly6e*), ependymal cells (*Tmem212* and *Ccdc153*) and choroid plexus (CP) epithelium cells (*Ttr* and *Enpp2*), along with other rarer populations (olfactory ensheathing cells, fibroblasts and GABA$^+$ neurons). A small contamination by microglia (*Hexb* and *Cx3cr1*) and red blood cells (*Hbb-bs* and *Hbb-bt*) was also detected and removed from downstream analysis. Overall, cell type composition and abundance were not altered in 5xFAD relative to WT (Extended Data Fig. 1f).

Next, we performed differential gene expression analysis among cells originating from 5xFAD or WT brains to determine to which extent each cellular population was affected by the disease. To precisely and robustly quantify the number of differentially expressed genes (DEG), we used a binomial regression-based approach that we previously described[19]. Strikingly, we found that mature myelinating oligodendrocytes were the most altered population (adjusted $P<0.01$) with 98 DEGs, and only 25% of the genes were also shared by other cell populations (Fig. 1c,d; DEGs in other cell types are shown in Supplementary Table 2). To validate that this observation was not a result of sampling bias of a high number of oligodendrocytes compared to other cell types, we performed a power analysis. We found that, even by sampling 1,700 oligodendrocytes (half of their original number), the number of DEGs was still higher than other cell types (Fig. 1e). Altogether, these results suggest that, in 5xFAD mice, oligodendrocytes display extensive transcriptional alterations.

Identification of a disease-associated oligodendrocyte state. Intrigued by the transcriptional changes observed in mature myelinating oligodendrocytes in 5xFAD mice, we next carried out a deeper molecular characterization of them in 5xFAD relative to WT. To enrich specifically for mature oligodendrocytes, we sorted galactosylceramidase-positive (GalC$^+$)[20] cells (Fig. 2a and Extended Data Fig. 2a,b). We sorted cells from 5xFAD mice at different ages ranging from 6 months to 24 months and used age-matched WT mice as controls. The sequenced cells were filtered and computationally pooled with the previously sequenced oligodendrocytes, resulting in a database of 13,572 high-quality cells (total mice—6–8 months: $n=4$ 5xFAD, 4 WT; 10–11 months: $n=6$ 5xFAD, 5 WT; 15 months: $n=3$ 5xFAD, 3 WT; 24 months: $n=4$ 5xFAD, 4 WT) (Extended Data Fig. 2c). Refined clustering analysis of these oligodendrocytes revealed 14 different subclusters, each characterized by a unique expression profile (Fig. 2b,c). We further analyzed whether any oligodendrocyte clusters are enriched in 5xFAD relative to WT. This analysis revealed that clusters 12 and 14 were enriched in 5xFAD brains relative to WT (Fig. 2d). Cluster 14, characterized by expression of *Ccl4* and *Lyz2* (Fig. 2b), originated solely from the 24-month-old 5xFAD mice, in which it represented between 9% and 30% of the oligodendrocytes (Extended Data Fig. 2d). In contrast, cluster 12 was found at all tested timepoints from 6 months to 8 months and onwards. This cluster represented between 5% and 15% of all oligodendrocytes in 5xFAD mice, depending on age, but did not exceed 5% in WT mice (Fig. 2e). This cluster was also distinctly separated from the rest of the oligodendrocytes in the UMAP (Fig. 2c). Because of its significant increase with the disease progression, we termed this transcriptional state "disease-associated oligodendrocytes" (DOLs). Interestingly, DOLs were detected long after the appearance of amyloid plaques and inflammation manifestation within the brain in this mouse model of AD[17] (around 9–10 months old). In contrast, disease-associated microglia (DAM) appear as early as 1–2 months after birth in this mouse model[9], highlighting the differential dynamics of response between microglia and oligodendrocytes.

Differential expression analysis between DOLs and the rest of the oligodendrocytes identified 26 genes significantly upregulated by DOLs (adjusted $P<0.01$ and $\log_2$ fold change ($\log_2$FC) >1; Fig. 2f), encompassing both genes related to immune signaling and non-immune-related genes. Immune-related genes included *Serpina3n*, a serine protease inhibitor related to immune proteases[21,22]; the complement component *C4b*; several major histocompatibility complex I (MHC-I) genes (H2-D1, H2-K1 and *B2m*); and the cytokine *Il33*, which was previously shown to be expressed by oligodendrocytes under acute injury[23]. Among the non-immune upregulated genes, several have been previously linked to neuroinflammation, such as *Klk6* (ref. [24]), *Sgk1* (ref. [25]) and the exosome-related CD9 and CD63 (refs. [26,27]). Of note, similar cells were recently identified by single-nucleus RNA sequencing (snRNA-seq)[11] (Extended Data Fig. 2e,f).

To investigate the signaling pathways and transcriptional circuits possibly controlling the induction of DOLs, we performed motif enrichment analysis for the DEGs using iRegulon[28]. The analysis pointed out three major transcription factor (TF) families: the Stat/Irf (normalized enrichment score (NES) = 5.4), YY1/NF-κB (NES = 6) and Sox9 (NES = 6) families (Fig. 2g). MHC-I genes and *C4b* were inferred to be regulated through Stat/Irf and YY1/NF-κB binding motifs, whereas non-immune genes (*Klk6* and *Sgk1*) were associated with the Sox9 TF, a key regulator of oligodendrocyte differentiation and maturation[29,30]. These results suggest that the DEGs associated with the DOL signature are likely to be induced by a limited set of TF circuits, including members of the NF-κB and Stat/Irf families.

DOLs are independent of the dementia's etiology. Because we identified the DOLs in the 5xFAD model, we pondered to what extent the observed signature is amyloidosis specific, given that the DOLs were detected long after plaque appearance. To this end, we re-analyzed a recently published dataset[31] containing hippocampal cells of WT and of two different mouse models of cognitive impairment, including a model of tauopathy (P301L), and a model which combines tauopathy and amyloidosis (PS2/APP/P301L) (three animals per group, 19–22 months old; Fig. 3a). The PS2/APP/P301L mouse model carries mutations in the presenilin 2 (PSEN2), amyloid precursor protein (APP) and microtubule-associated protein tau (MAPT) genes. Among the 66,002 cells that passed quality control, a first round of analysis allowed identification of a large diversity of brain cells, including highly abundant oligodendrocytes (*Mbp* and *Plp1*, $n=30{,}787$), microglia (*Cx3cr1* and *Hexb*, $n=13{,}508$), astrocytes (*Slc1a2*, $n=3{,}303$), endothelial cells (*Cldn5*, $n=3{,}262$), neurons (*Nrgn*, $n=2{,}252$), Cajal–Retzius cells (*Reln* and *Nhlh2*, $n=1{,}787$), T cells (*Cd3d*, $n=1{,}263$), pericytes (*Kcnj8*, $n=1{,}149$), ependymal cells (*Tmem212*, $n=841$), vascular smooth muscle cells (*Acta2*, $n=455$), vascular leptomeningeal cells (*Slc22a6* and Inmt, $n=312$), neuronal progenitor cells (*Tubb5* and *Smc2*, $n=188$) and CP epithelial cells (*Ttr*, $n=108$) (Extended Data Fig. 3a,b). The large number of oligodendrocytes in this dataset allowed us to perform a detailed analysis of this compartment, resulting in the identification of 13 different clusters (Fig. 3b). Interestingly, one of those clusters (cluster 11) was characterized by the upregulation of several characteristic DOL genes, including *Serpina3n* (highest upregulation with $\log_2$FC = 5.8), *Klk6* ($\log_2$FC = 4.76), *C4b* ($\log_2$FC = 3.83), H2-D1 ($\log_2$FC = 1.7) and *Cd9* ($\log_2$FC = 1.8) (Fig. 3c). To further validate that this cluster corresponds to DOLs, we performed a gene set enrichment analysis (GSEA). We observed a highly significant enrichment of DOL genes among the upregulated genes of cluster

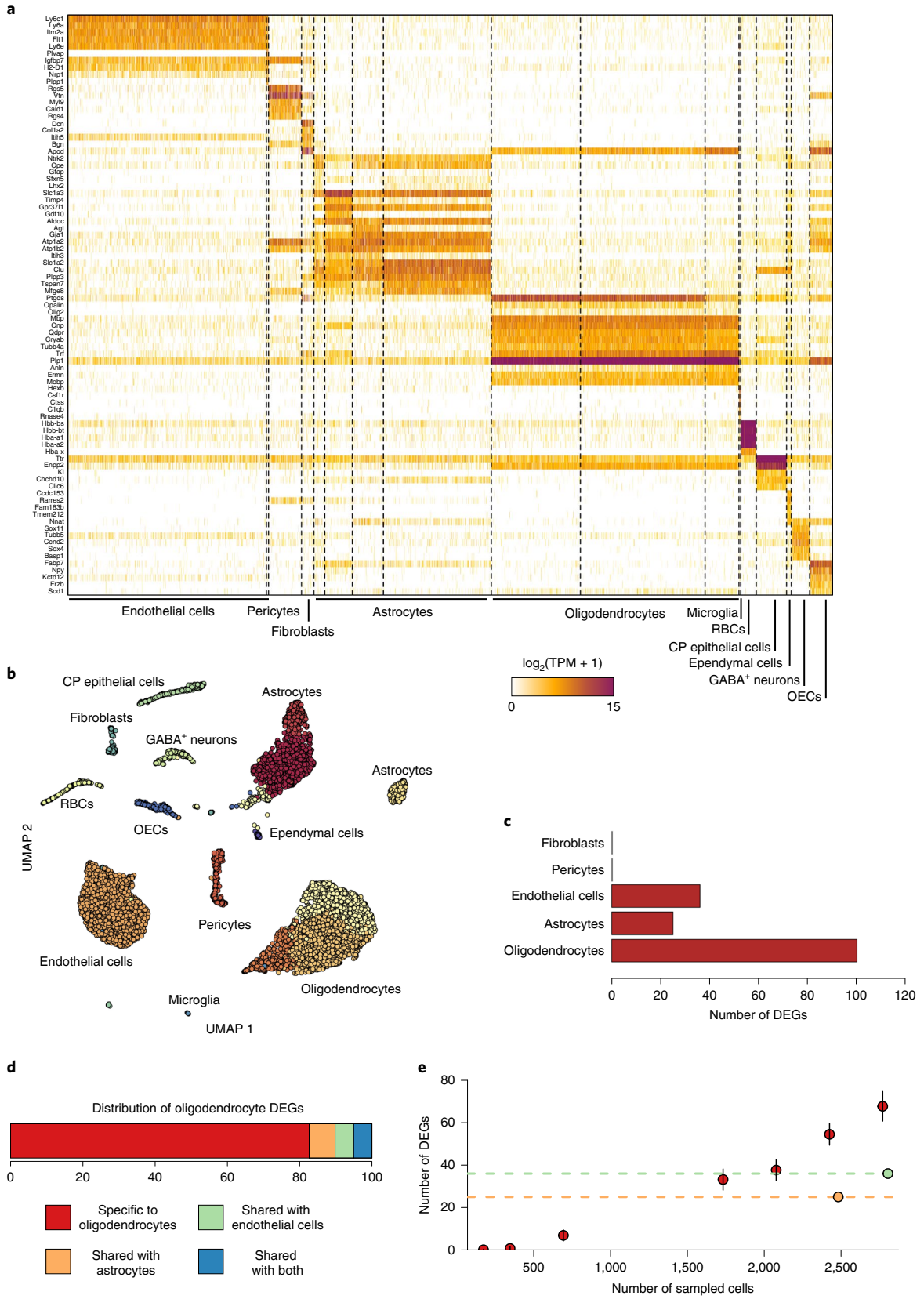

Fig. 1 | Oligodendrocytes display major transcriptomic alterations in the 5xFAD mouse model. a, Single-cell expression heat map of non-immune (CD45$^-$) cells from 5xFAD ($n=9$) and WT ($n=9$) mice. **b**, Two-dimensional uniform manifold approximation and projection (UMAP) embedding of the scRNA-seq data. Dots are colored based on the scRNA-seq clustering. **c**, Number of DEGs between 5xFAD and WT mice across the major cell types. **d**, Specificity of the DEGs in oligodendrocytes. **e**, Power analysis—number of DEGs based on the number of cells used for the differential expression analysis. Red, downsampling of oligodendrocytes; orange, astrocytes; green, endothelial cells. Red dots correspond to the mean number of DEGs, and the bar represents the standard deviation. RBC, red blood cell. OEC, olfactory ensheathing cell.

11 (NES = 1.85, $P = 1.0 \times 10^{-5}$) (Fig. 3d), further confirming that those cells are similar to DOLs. In this dataset and in line with our results, DOLs could be barely identified in WT mice but were found in both pure tauopathy (P301L) and a combined tauopathy/amyloidosis model (PS2/APP/P301L), suggesting that DOLs are not specific to the 5xFAD model or amyloidosis (Fig. 3e). Refined analysis of the microglia compartment revealed 11 different clusters, with two of them expressing typical DAM genes, such as *Dkk2* and *Cst7* (Extended Data Fig. 3c). Of note, DAM, unlike DOLs, were not found in the model of pure tauopathy (Fig. 3f), highlighting that the oligodendrocytes' response, unlike microglia, is not Aβ specific.

To further substantiate our finding that DOLs are not induced directly by Aβ accumulation, we generated mouse primary cell cultures of mature myelinating oligodendrocytes and treated them with $A\beta_{1-42}$ in different aggregation states—oligomers, fibrils and plaques[32]—followed by RNA-seq. We did not observe upregulation of DOL signature genes after the treatment compared to scramble-treated controls (Fig. 3g and Extended Data Fig. 3d), further supporting the contention that Aβ does not lead directly to oligodendrocyte activation or that Aβ is not sufficient. Altogether, the DOL appearance late after Aβ accumulation and the lack of response to Aβ in vitro suggest that the presence of DOLs in the 5xAD is independent of the primary cause of dementia and might represent oligodendrocytes' response to damage within the CNS.

DOL signature in non-AD pathologies. Based on the above results, we hypothesized that the DOLs identified in amyloidosis and tauopathy models might be found in other chronic CNS pathologies beyond dementia. To test this hypothesis, we conducted a meta-analysis of three previously published mouse scRNA-seq datasets (Fig. 4a). Two of the datasets were from the spinal cord of experimental autoimmune encephalomyelitis (EAE), an experimental model of multiple sclerosis (MS)[33]. MS and EAE are characterized by a massive inflammation resulting from infiltration of adaptive immune cells into the CNS and cytotoxic effect on oligodendrocytes, resulting in their death and de-myelination. EAE is multi-phasic, characterized by a phase of gradually worsening symptoms (priming), up to a peak in both inflammation and clinical condition, mostly followed by a reduction in disease severity and inflammation, resulting in improved clinical symptoms (remission)[34]. The first dataset was derived from the spinal cord of mice in the peak stage of EAE[35], compared to spinal cord of control mice injected with complete Freund's adjuvant (CFA). The second dataset, also from EAE mouse spinal cord, included data from the different phases of EAE: priming, peak and remission and CFA-injected control[36]. Lastly, the third dataset was generated from the subventricular zone (SVZ) of young (3 months old) and old (28–29 months old) mice[37]. We analyzed these datasets using the Pagoda2 pipeline. All datasets were rich in oligodendrocytes (1,207, 2,552 and 4,683 oligodendrocytes identified, respectively), making them appropriate for our analysis. We first computationally gated oligodendrocytes and looked for DEGs between pathogenic and non-pathogenic samples (Fig. 4a). In all three datasets, we found expression of pathology-associated genes in oligodendrocytes (Fig. 4b-d), significantly enriched in DOL characteristic genes as revealed by GSEA (Extended Data Fig. 4a–c). Interestingly, some variations in the DOL signature were observed across conditions. For instance, *C4b* was upregulated in the acute EAE and aging models but not in multi-phasic EAE, whereas MHC-I genes were upregulated in both EAE models but not in aging (Fig. 4b–d). We also found that the expression level of DOL signature was linked to EAE disease course; the expression level was elevated during the priming phase, reached its maximum at the peak phase and gradually reduced during remission (Fig. 4e). These results suggest that the intensity of the oligodendrocyte response correlates with disease severity and likely with the intensity of inflammation.

Non-immune glial cells, mainly astrocytes, were previously reported to respond to systemic inflammation triggered by lipopolysaccharide (LPS) by altering their gene expression, a state described as 'reactive astrocytes'[38]. A similar astrocytic profile was also later observed in 5xFAD mouse hippocampus, the disease-associated astrocytes (DAAs)[10]. Interestingly, DAA and DOL transcriptomic signatures partially overlap, as both include *Serpina3n*, H2-D1, *B2m* and *C4b* genes. A recently published study investigated the spatial transcriptome of mouse brain sections after systemic LPS injection using the Visium platform from 10x Genomics[39]. We were intrigued whether, in this experimental setting, a DOL-like response is induced, as we found in the neuroinflammatory settings in the mouse brain, and we tested its co-localization with oligodendrocyte markers. We first performed an unsupervised demultiplexing of the data using topic modeling (Methods): using this approach, we identified a topic (topic number 8)—that is, a latent dimension—that was strongly expressed in the LPS-stimulated samples (S1, S2 and S6) but not in control samples (S3, S4 and S7) (Extended Data Fig. 4d). Notably, the genes most significantly contributing to this dimension included several members of the DOL signature (Extended Data Fig. 4e), prompting us to call this dimension the DOL-like signature. *Serpina3n* expression was significantly higher in LPS-treated mice than in control animals (Extended Data Fig. 4f). Spatially, the DOL-like response was observed in regions surrounding the 3rd and lateral ventricles, suggesting that factors carried by the cerebrospinal fluid might be, at least partially, mediating this response (Fig. 4f). We examined if the observed DOL-like topic is associated with oligodendrocyte topic. We identified topic number 2 as enriched in oligodendrocyte markers (high contribution of *Plp1*, *Mbp* and *Mog* genes), and its spatial pattern across sections corresponded to the expected spatial distribution of white matter (Extended Data Fig. 4g). Correlation between the intensity of the two topics was low ($R^2 = 0.0017$), suggesting that the DOL-like signature also included the response of other cell types. Indeed, among the top genes contributing to this topic, we found several markers of astrocyte activation, such as *Gfap* and *Gja1*, suggesting that the DOL-like response is also shared by activated astrocytes in systemic LPS challenge.

Our meta-analysis further substantiated the notion that the DOL response is a conserved response of oligodendrocytes to pathological deviation from CNS homeostasis, which might be relevant to

Fig. 2 | Identification of a disease-associated oligodendrocyte state. a, Experimental strategy to study oligodendrocytes. Illustration was created with BioRender. **b**, Expression heat map of oligodendrocytes from 5xFAD and WT mice at various ages, GalC$^+$ sorted and pooled together with the previously sequenced oligodendrocytes. $n = 33$ independent mice (across ages—6–8 months: $n = 4$ 5xFAD, 4 WT; 10–11 months: $n = 6$ 5xFAD, 5 WT; 15 months: $n = 3$ 5xFAD, 3 WT; 24 months: $n = 4$ 5xFAD, 4 WT). **c**, Two-dimensional UMAP embedding of the scRNA-seq oligodendrocyte data. Dots are colored based on the scRNA-seq clustering. Top, cells from WT mice; bottom, cells from 5xFAD mice. **d**, Z-score of the enrichment test comparing cluster frequency between 5xFAD and WT mice. *P* values were computed by fitting a Poisson regression and corrected using multiple testing (Methods). **e**, Proportion of DOLs among oligodendrocytes between 5xFAD and WT mice (left panel) and across ages (right panel). *P* values were computed using the Kruskal–Wallis test. Large bars correspond to the median and small bars to the interquartile range (IQR). $n = 33$ independent mice (across ages—6–8 months: $n = 4$ 5xFAD, 4 WT; 10–11 months: $n = 6$ 5xFAD, 5 WT; 15 months; $n = 3$ 5xFAD, 3 WT; 24 months: $n = 4$ 5xFAD, 4 WT). **f**, Volcano plot corresponding to the differential expression analysis between DOLs and the rest of the oligodendrocytes. **g**, Results of the promoter analysis by iRegulon. FDR, false discovery rate; TPM, transcripts per million..

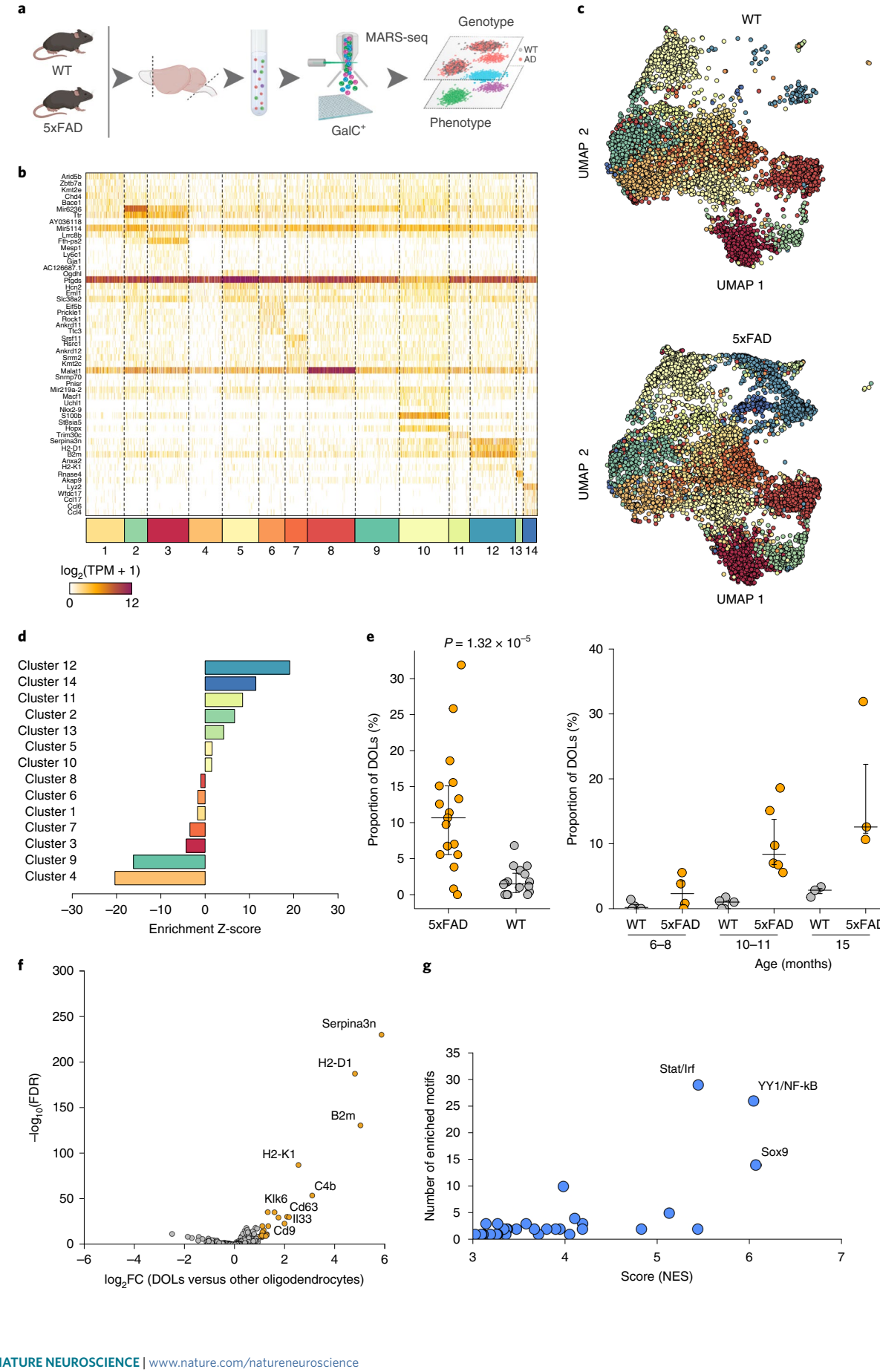
a
WT
5xFAD
MARS-seq
GalC+
Genotype
WT
AD
Phenotype
b
log2(TPM + 1)
0
12
1 2 3 4 5 6 7 8 9 10 11 12 13 14
c
WT
UMAP 2
UMAP 1
5xFAD
UMAP 2
UMAP 1
d
Cluster 12
Cluster 14
Cluster 11
Cluster 2
Cluster 13
Cluster 5
Cluster 10
Cluster 8
Cluster 6
Cluster 1
Cluster 7
Cluster 3
Cluster 9
Cluster 4
−30 −20 −10 0 10 20 30
Enrichment Z-score
e
P = 1.32 × 10−5
Proportion of DOLs (%)
5xFAD
WT
Proportion of DOLs (%)
WT 5xFAD WT 5xFAD WT 5xFAD WT 5xFAD
6–8 10–11 15 24
Age (months)
f
−log10(FDR)
Serpina3n
H2-D1
B2m
H2-K1
C4b
Klk6
Cd63
Il33
Cd9
log2FC (DOLs versus other oligodendrocytes)
g
Number of enriched motifs
Stat/Irf
YY1/NF-kB
Sox9
Score (NES)

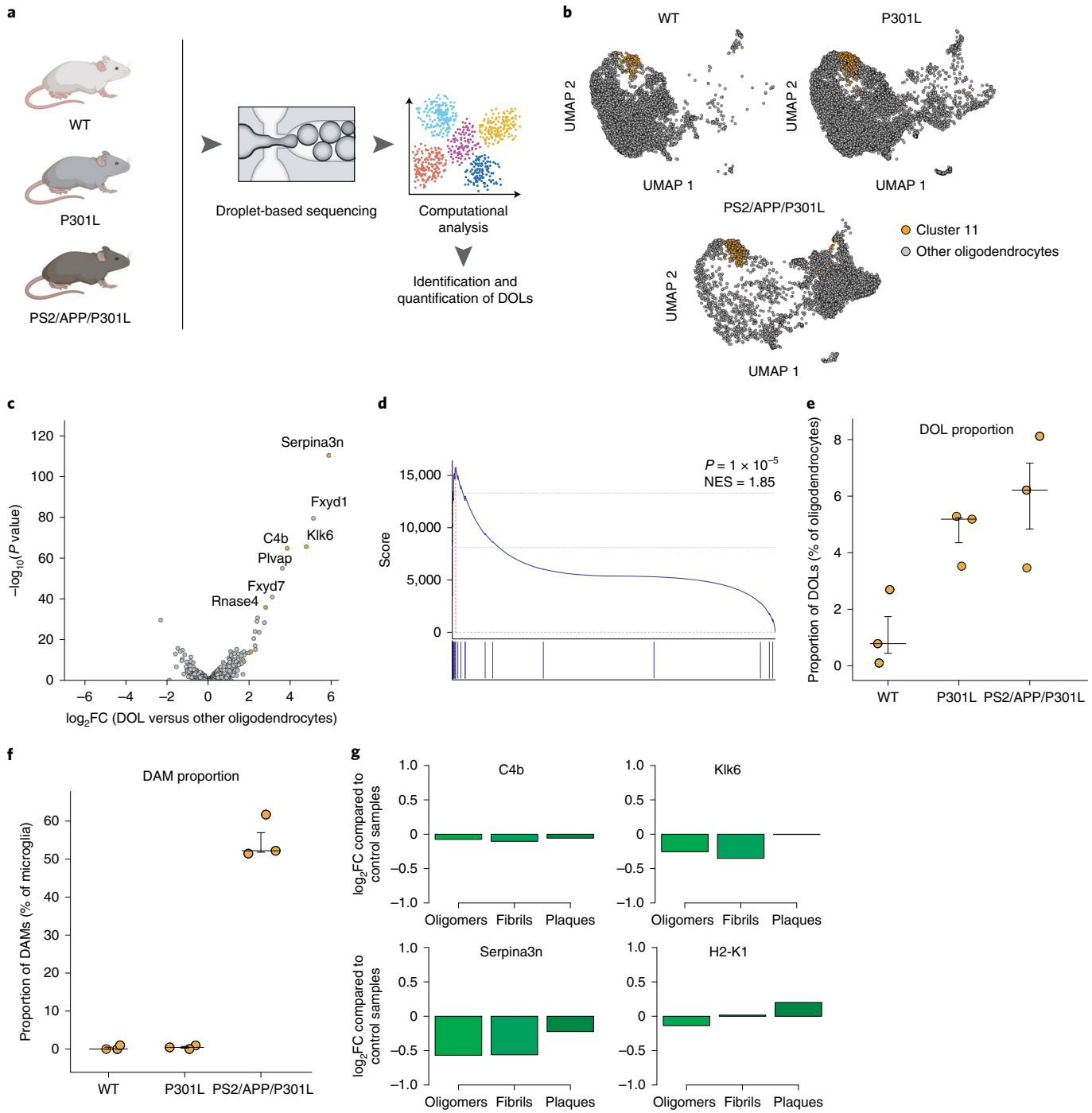

Fig. 3 | DOLs are independent of the dementia's etiology. a, Experimental strategy in the scRNA-seq dataset from Lee et al.[31]. **b**, Two-dimensional UMAP embedding of the oligodendrocytes in each mouse model. Cluster 11 cells are in orange. **c**, Comparison of the mean transcriptional profile of oligodendrocytes from cluster 11 with the rest of the oligodendrocytes. DOL genes are colored in orange. **d**, Result of GSEA analysis performed on the log_2FC list between oligodendrocytes from cluster 11 and the rest of the oligodendrocytes using the DOL genes as a query gene set. *P* values were computed by performing a GSEA as described by Subramanian et al.[56]. **e**, Proportion of DOLs among oligodendrocytes across mouse strains ($n=3$ for each strain). Large bars correspond to the median and small bars to the IQR. **f**, Proportion of DAM among microglia across mouse strains ($n=3$ for each strain). Large bars correspond to the median and small bars to the IQR. **g**, log_2FC of DOL genes in cultured oligodendrocytes after treatment with Aβ at different aggregation stages.

multiple diseases beyond AD. Furthermore, the overlap between the signatures of DOLs and of reactive astrocytes suggests a common response module of non-immune glia.

Spatial analysis of DOLs in mouse and human brain sections. Next, we studied the spatial distribution of DOLs in the mouse model of amyloidosis, the 5xFAD brain. As a proxy to the DOL signature, we used the protein marker SERPINA3N, encoded by the most prominent gene associated with the DOL state, *Serpina3n*. We first analyzed by immunofluorescence and confocal microscopy coronal sections from 16-month-old 5xFAD mouse brains stained for OLIG2 (oligodendrocyte-lineage nuclear marker), SERPINA3N

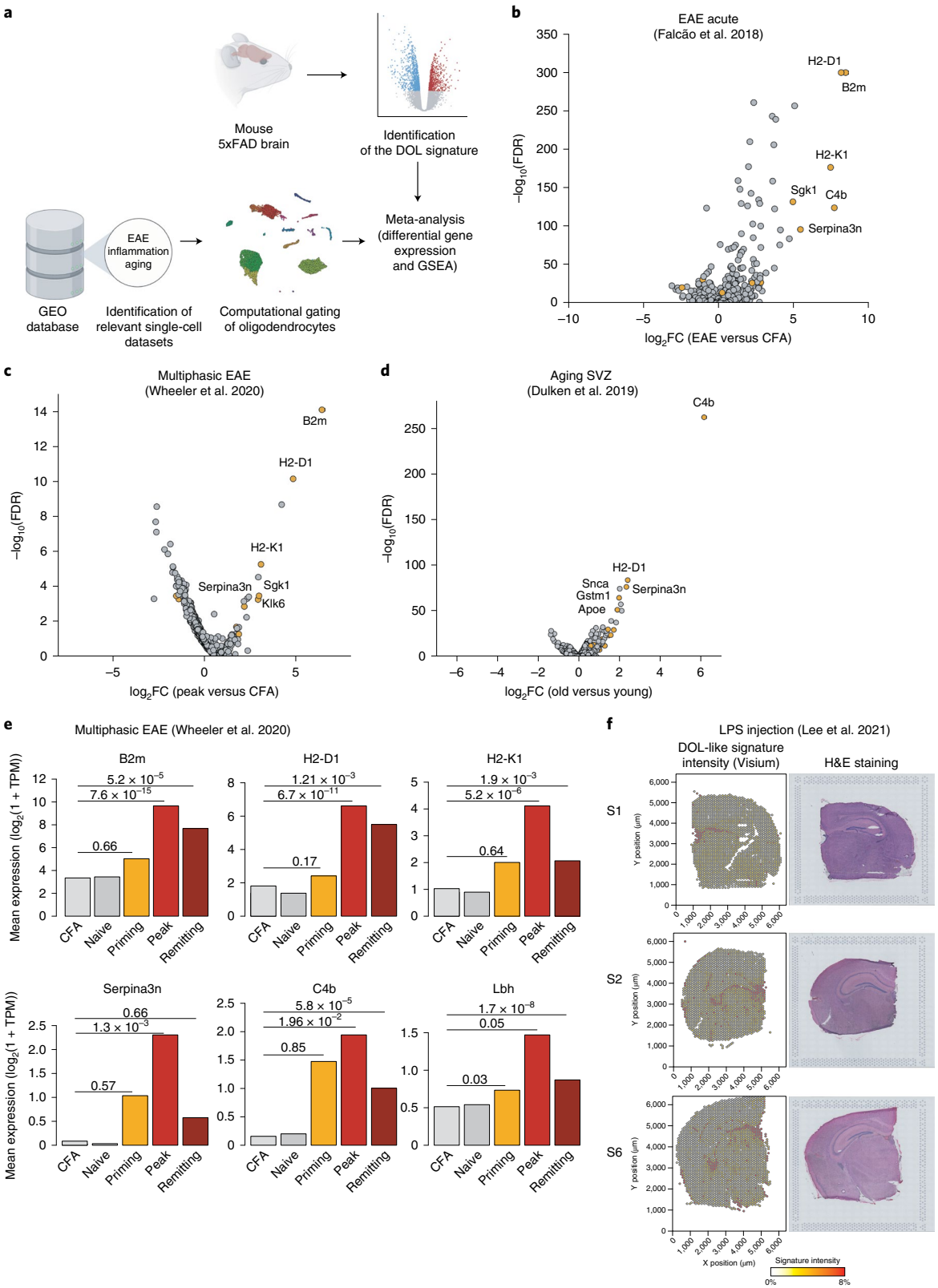

Fig. 4 | DOL signature in non-AD pathologies. a, Analytical approach used to identify DOL signature in additional CNS pathologies. **b**, Volcano plot corresponding to the differential expression analysis between oligodendrocytes from control (CFA) and EAE spinal cord (Falcão et al.[35]). DOL genes are colored in orange. **c**, Volcano plot corresponding to the differential expression analysis between oligodendrocytes from control (CFA) and peak EAE spinal cord (Wheeler et al.[36]). DOL genes are colored in orange. **d**, Volcano plot corresponding to the differential expression analysis between oligodendrocytes from young and old mice (Dulken et al.[37]). DOL genes are colored in orange. **e**, Kinetics of the mean expression level of key DOL genes across various EAE stages. *P* values were computed using a binomial regression with complementary log–log link function (Methods). **f**, Intensity of the DOL-like signature across the sections of the three LPS-treated mice (left). Hematoxylin and eosin (H&E) staining of the corresponding slides (right). FDR, false discovery rate; TPM, transcripts per million.

and human Aβ (amyloid plaques). We found OLIG2$^+$SERPINA3N$^+$ double-positive cells (Fig. 5a and Extended Data Fig. 5a, white arrows) in areas of damage (enriched with Aβ plaques), whereas no SERPINA3N signal was observed in the WT brain. To perform an extensive and quantitative spatial analysis, we used the same cohort of 16-month-old 5xFAD ($n=4$) and WT ($n=2$) mice, stained coronal brain sections for OLIG2 as well as for SERPINA3N and Aβ plaques and analyzed them by scanning a large area (on average, 11.5 mm^2) of the cerebral cortex, using a slide scanner. To automatically detect cells, we used the recently published tool DeepCell[40]. Plaques were detected using a classical watershed-based segmentation approach (Methods) (Fig. 5b). A total of 309,333 cells were analyzed. To validate the method used for the analysis, we performed quality controls, which ruled out bias of cell size or OLIG2 intensity across samples (Extended Data Fig. 5b,c). By automated thresholding, we confirmed a highly homogeneous proportion of OLIG2$^+$ cells across samples (Extended Data Fig. 5d,e) and a limited number of false-positive Aβ plaques detected in the WT (<50) (Extended Data Fig. 5f). We then proceeded to analyze SERPINA3N immunoreactivity. Automated thresholding of SERPINA3N intensity (Extended Data Fig. 5g) revealed a high frequency of SERPINA3N$^+$ cells in 5xFAD mice but not in WT mice (Fig. 5c), a pattern that could also be observed among OLIG2$^+$ cells (Fig. 5d). To assess the spatial distribution of OLIG2$^+$SERPINA3N$^+$ cells, we computed the Besag's L function[41] of these cells in each of the examined 5xFAD brains (Fig. 5e). In brief, the L function describes the mean number of pairs of points (that is, pairs of OLIG2$^+$SERPINA3N$^+$ cells) at a given radius (r). For a given r, a positive or negative value corresponds to a 'higher than expected' or 'lower than expected' number of pairs, respectively, compared to a random spatial distribution. We observed highly similar profiles across the four tested brains, with positive values of the L function between 10 µm and 300 µm, with a peak around 50–70 µm, validating that OLIG2$^+$SERPINA3N$^+$ cells are not randomly distributed across the cortex but appear in discrete areas. Such a distribution of OLIG2$^+$SERPINA3N$^+$ cells argued in favor of association of these cells with tissue damage and prompted us to examine their spatial association with areas of plaques, which are known to be the sites of damage in this model[42–46].

To examine the association between OLIG2$^+$SERPINA3N$^+$ cells and plaques, we fitted a penalized spatial Gibbs point pattern model, termed PenGE[47]. In brief, we provided a list of range values (30 µm, 80 µm, 160 µm and 300 µm), and PenGE estimated the most likely potential energy function between subjects of interest, under the form of a stepwise function, where a positive value corresponds to an 'attraction' and a negative value to a 'repulsion'. After also verifying by this analysis that OLIG2$^+$SERPINA3N$^+$ cells are not randomly distributed (Fig. 5f, blue), we analyzed the spatial interaction between OLIG2$^+$SERPINA3N$^+$ cells and plaques. We found a positive interaction in ranges below 30 µm (Fig. 5f, red) in all tested brains. This analysis, therefore, suggests that the spatial distribution of OLIG2$^+$SERPINA3N$^+$ cells could be linked to damage areas (enriched with plaques).

Although mouse oligodendrocytes with a similar transcriptomic signature to DOLs were previously identified using snRNA-seq, no evidence of such cells was reported in humans using the same technique[11,48]. Indeed, snRNA-seq was shown to have lower sensitivity, rendering it unsuitable for detecting many activation-related genes[49]. To further examine whether DOL signature could be relevant to human AD, we re-analyzed spatial transcriptomic data of postmortem human brain sections from the middle temporal gyrus[50]. Similarly to the analysis of the mouse Visium samples, we performed a topic modeling approach and identified two topics that were specifically expressed by one of the two AD samples (Fig. 5g). Analysis of the most contributing genes revealed that the first topic was associated with macrophage-specific and microglia-specific genes (*C1QC*, *C1QA*, *AIF1* and *FCER1G*) (Extended Data Fig. 5h), whereas *SERPINA3* was the most contributing gene of the second topic, together with several inflammatory genes, such as *CHI3L1*, *VSIG4* and *SOD2* (Extended Data Fig. 5i). The macrophage signature displayed a highly clustered pattern (Fig. 5h, middle panel), whereas the inflammatory topic was more spatially dispersed (Fig. 5h, right panel). The inflammatory topic intensity was higher in the margins of high macrophage regions. These results suggested that the expression of DOL key genes, such as SERPINA3, could be relevant in human AD.

To detect oligodendrocytes that express key features of DOLs in human AD, we analyzed by immunohistochemistry postmortem brain samples from patients with AD ($n=8$) and age-matched non-demented controls (NDCs, $n=8$). The patients' disease description is shown in Supplementary Table 3. We imaged a 20-mm^2 area of the temporal cortex, containing both gray matter and white matter. As in the mice, we used SERPINA3 (the human homolog of SERPINA3N) and CC1, an oligodendrocyte-specific marker[51], together with thioflavin-S (intracellular and extracellular Aβ). Confocal imaging revealed the presence of SERPINA3$^+$CC1$^+$ cells in the gray matter of the temporal cortex of postmortem AD patients but not in NDC (Fig. 5i and Extended Data Fig. 5j). To quantify the incidence of SERPINA3$^+$ cells, we applied the same

Fig. 5 | Spatial analysis of DOLs in mouse and human brain sections. Immunohistochemistry of DOL-like cells and analysis of spatial association with areas enriched with plaques in 5xFAD mice (**a**–**f**). **a**, Representative image of DOLs (OLIG2$^+$ (red) SERPINA3N$^+$(cyan)) from cortex of 16-month-old 5xFAD and WT mice. In 5xFAD, DOLs are in proximity to Aβ plaques (yellow); magnification ×63, and scale bar corresponds to 20 µm. Arrowheads point to OLIG2$^+$SERPINA3N$^+$ cells. **b**, Description of the experimental and computational approach used to study DOL location in mouse and human brains. Illustration was created with BioRender. **c**, Proportion of SERPINA3N$^+$ cells in 5xFAD ($n=4$) and WT ($n=2$) mice. Large bars correspond to the median and small bars to the IQR. **d**, Proportion of SERPINA3N$^+$ cells among OLIG2$^+$ cells in 5xFAD and WT mice. Large bars correspond to the median and small bars to IQR. **e**, Normalized L functions of the SERPINA3N$^+$OLIG2$^+$ cells in 5xFAD sections. Each curve corresponds to a unique sample. **f**, Estimated interaction functions within SERPINA3N$^+$OLIG2$^+$ cells (blue curves) or between them and plaques (red curves) in 5xFAD mice. Each curve corresponds to a unique sample. Analysis of Visium data from postmortem human AD brains (**g**,**h**). **g**, Intensity of the macrophage (left) and inflammatory (right) topics across the four samples. $n=4$ biologically independent samples (two AD and two NDC). The thick line corresponds to the median, and the bottom and upper limits of the box correspond to the first and third quartiles, respectively. The lower and upper whiskers correspond to the lowest and highest values, respectively, within the range of the first (third) quartile minus (plus) 1.5 times the IQR. **h**, H&E staining of the AD2 sample (left panel), spatial pattern of the macrophage (middle panel) and inflammatory (right panel) topics. Immunohistochemistry of postmortem human AD brains (**i**–**k**). **i**, Representative image of postmortem AD patient (right) and NDC (left) temporal cortex stained for oligodendrocyte marker (CC1, red), SERPINA3 (cyan), Aβ (thioflavin S, yellow) and nuclei (Hoechst, blue); magnification ×20, and scale bar corresponds to 50 µm. Arrowheads point to CC1$^+$SERPINA3$^+$ cells. Inset marks the position of the right image in ×63 magnification, and scale bar corresponds to 20 µm. **j**, Proportion of SERPINA3N$^+$ cells in AD ($n=8$) and NDC ($n=8$) samples. Large bars correspond to the median and small bars to the IQR. *P* values were computed using a Wilcoxon rank test. **k**, Association between MMSE score and proportion of SERPINA3$^+$ cells. The dashed line corresponds to an ordinary least square linear. *P* values were computed by testing the significance of the contribution of the MMSE score to predict the proportion of SERPINA3$^+$ cells using a likelihood ratio test (LRT). CNN, convolutional neural network.

approach as for the mouse sections, using our image analysis pipeline (Fig. 5b and Extended Data Fig. 5k), and a total of 475,091 cells were analyzed. Automatic thresholding of SERPINA3 intensity (Extended Data Fig. 5l) confirmed the significant enrichment ($P=0.027$) of SERPINA3$^+$ cells in postmortem AD compared to NDC sections (Fig. 5j). Interestingly, we observed a significant correlation ($P=0.0043$ and $R^2=0.50$) between the proportion of SERPINA3$^+$ cells and the Mini-Mental State Examination (MMSE) score (Fig. 5k), suggesting that SERPINA3 might serve as a quantitative marker of AD-induced cognitive impairment.

Overall, using spatial transcriptomics and immunohistochemistry, we identified SERPINA3N and SERPINA3 in mice and humans, respectively, as key markers of non-immune glia activation in AD.

Discussion

In this work, using scRNA-seq, we identified an oligodendrocyte cell state (DOLs) that represents a shared transcriptomic module emerging in response to deviation from CNS homeostasis. This transcriptomic module seems to be common across different pathological states, and elements of it are potentially relevant to human diseases.

In the 5xFAD mouse model of amyloidosis, DOLs appear around 10 months of age, after numerous pathological events that occur earlier in the brains of these mice, including Aβ plaque accumulation, gliosis, inflammation and cognitive impairments[17]. These results suggest that the oligodendrocyte response to damage in 5xFAD is late relative to other non-neuronal cells, such as microglia

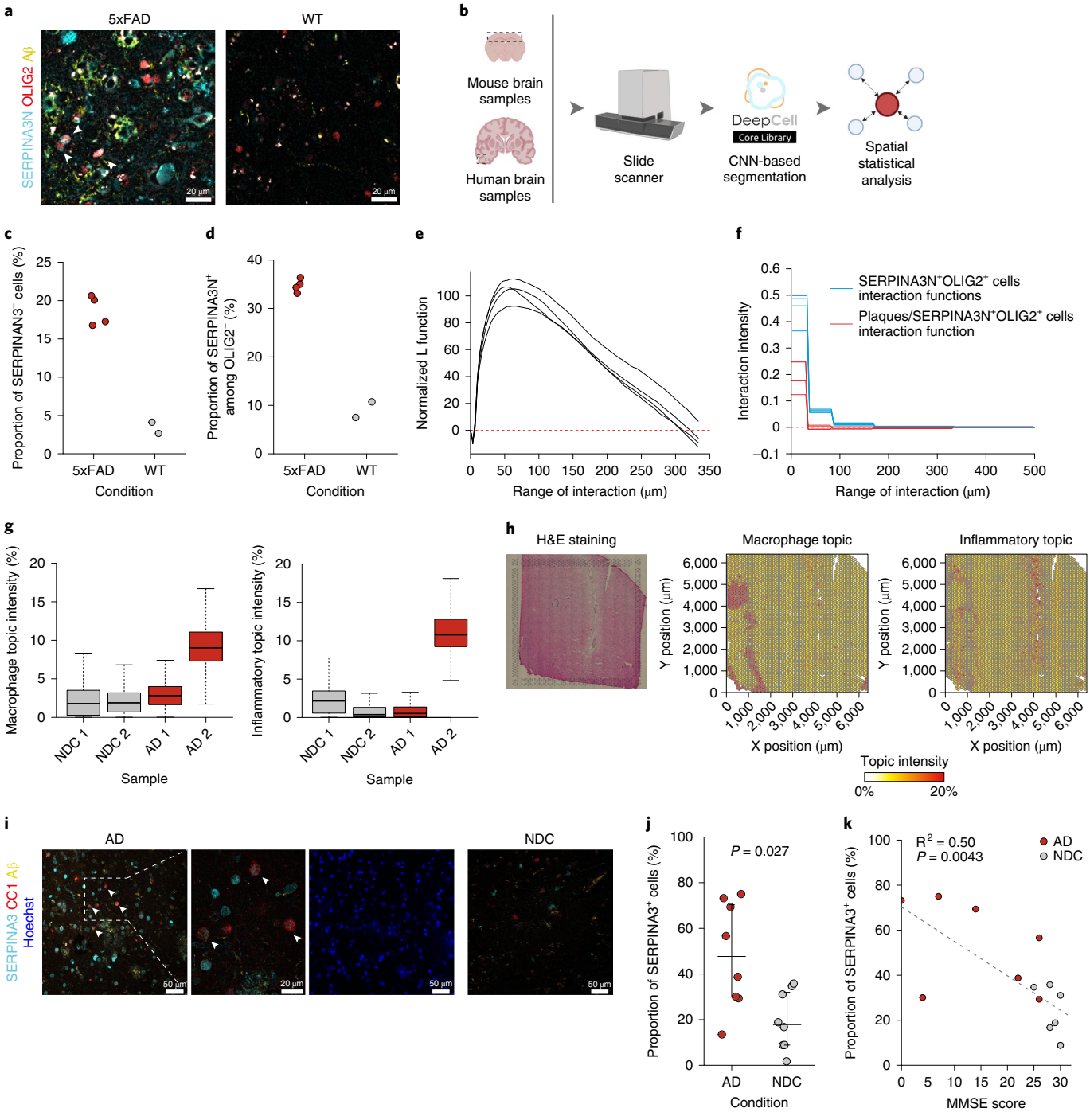

and astrocytes[9,10], indicating that it might be a consequence of accumulated damage.

Although DOLs were found in proximity to Aβ plaques, their appearance long after plaque accumulation, together with our in vitro results that revealed that Aβ by itself is not sufficient to induce them, and the fact that they were also found in models that do not exhibit amyloidosis, argue against Aβ as a sufficient trigger of this cellular state. However, their presence in brain areas enriched with plaques suggests an involvement of additional factors, such as damage-associated molecular patterns (DAMPs)[52], the release of various metabolic factors from dying cells and inflammation. Transcriptomic alterations similar to DOL signature were also observed by spatial transcriptomics of the plaque niche[43] in a different model of amyloidosis, further supporting the notion that the plaque microenvironment is enriched in factors contributing to this cellular state.

In EAE, oligodendrocyte precursor cells (OPCs) and mature oligodendrocytes with a similar signature have been shown to acquire phagocytic abilities, present antigens on MHC-II and activate CD4 T cells[35]. In 5xFAD, unlike in EAE, by in-depth analysis of the transcriptomic profile of mature oligodendrocytes ($GalC^+$) by scRNA-seq, we observed upregulation of MHC-I pathway only and not MHC-II, implying that interaction with CD8 T cells might be more likely than with CD4 T cells. However, we cannot exclude the possibility that alterations like the ones observed in EAE are occurring in OPCs in AD. Moreover, a recent study suggested that OPCs might become senescent in the context of amyloidosis[53]. In mature oligodendrocytes, we have not found evidence for any senescence markers at the transcriptomic level. However, further in-depth characterization of OPCs will be required to answer these questions. In line with our observations in the 5xFAD model, the expression level of DOL genes in EAE was found to be increased with disease progression, further supporting a relationship between damage accumulation and DOL signature expression. These observations support the general name given to this oligodendrocyte state—disease-associated—regardless of the nature of the etiology.

The overlap in transcriptomic signature between DOLs and DAAs, which were reported across several conditions[10,38,39,43,54], suggests that, despite fundamental differences in function between astrocytes and oligodendrocytes, they share similar molecular pathways of response to damage (for example, upregulation of *Serpina3n*, *C4b* and *Ctsb*). Microglial responses seem to be more pathology specific, as in the case of DAM, which are observed in amyloidosis but not in tauopathy[9,31]. Of note, within the common signature of astrocytes and the oligodendrocytes, some genes were also found in microglia—for example, *C4b*[55]. Further in-depth study will be required to determine the functions that these responses serve and how they may be targeted in developing effective therapeutics for CNS pathologies.

Using immunohistochemistry, we detected $SERPINA3^+$ oligodendrocytes in human postmortem AD brains. Spatial transcriptomics revealed high intensity of *SERPINA3* signature associated with inflammation in proximity to macrophages, further supporting the contention that *SERPINA3* expression is potentially induced by inflammation and damage. However, the fact that we used a single marker in the immunohistochemistry and that spatial transcriptomics lacks single-cell resolution prevented us from fully characterizing these cells to determine the degree of similarity to mouse DOLs. We also showed a correlation between the proportion of $SERPINA3^+$ cells in the brain and the MMSE score, suggesting that SERPINA3 may serve as a biomarker of cognitive impairment. Of note, *Serpina3n* was shown to inhibit granzyme B[22], therefore protecting cells from cytotoxic death induced by CD8 T cells. In addition, it was shown to promote plaque aggregation in vitro[11]. Therefore, further studies are necessary to elucidate the role of DOLs, and *Serpina3n/SERPINA3* in particular, and their relevance to human diseases.

In summary, our work shows the common molecular pathways that oligodendrocytes acquire in different neurodegenerative conditions and highlights the potential of targeting these common pathological mechanisms underlying CNS diseases.

Online content

Any methods, additional references, Nature Research reporting summaries, source data, extended data, supplementary information, acknowledgements, peer review information; details of author contributions and competing interests; and statements of data and code availability are available at https://doi.org/10.1038/s41593-022-01104-7.

Received: 21 July 2021; Accepted: 19 May 2022;
Published online: 27 June 2022

References

1. Masters, C. L. et al. Alzheimer's disease. *Nat. Rev. Dis. Prim.* **1**, 15056 (2015).
2. Holtzman, D. M., Morris, J. C. & Goate, A. M. Alzheimer's disease: the challenge of the second century. *Sci. Transl. Med.* **3**, 77sr1 (2011).
3. Reitz, C. & Mayeux, R. Alzheimer disease: epidemiology, diagnostic criteria, risk factors and biomarkers. *Biochem. Pharmacol.* **88**, 640–651 (2014).
4. Karch, C. M. & Goate, A. M. Alzheimer's disease risk genes and mechanisms of disease pathogenesis. *Biol. Psychiatry* **77**, 43–51 (2015).
5. Schwartz, M. & Deczkowska, A. Neurological disease as a failure of brain–immune crosstalk: the multiple faces of neuroinflammation. *Trends Immunol.* **37**, 668–679 (2016).
6. Heneka, M. T. et al. Neuroinflammation in Alzheimer's disease. *Lancet Neurol.* **14**, 388–405 (2015).
7. Wyss-Coray, T. & Rogers, J. Inflammation in Alzheimer disease—a brief review of the basic science and clinical literature. *Cold Spring Harb. Perspect. Med.* **2**, a006346 (2012).
8. De Strooper, B. & Karran, E. The cellular phase of Alzheimer's disease. *Cell* **164**, 603–615 (2016).
9. Keren-Shaul, H. et al. A unique microglia type associated with restricting development of Alzheimer's disease. *Cell* **169**, 1276–1290 (2017).
10. Habib, N. et al. Disease-associated astrocytes in Alzheimer's disease and aging. *Nat. Neurosci.* **23**, 701–706 (2020).
11. Zhou, Y. et al. Human and mouse single-nucleus transcriptomics reveal TREM2-dependent and TREM2-independent cellular responses in Alzheimer's disease. *Nat. Med.* **26**, 131–142 (2020).
12. Nasrabady, S. E., Rizvi, B., Goldman, J. E. & Brickman, A. M. White matter changes in Alzheimer's disease: a focus on myelin and oligodendrocytes. *Acta Neuropathol. Commun.* **6**, 22 (2018).
13. Wu, Y. et al. Alterations of myelin morphology and oligodendrocyte development in early stage of Alzheimer's disease mouse model. *Neurosci. Lett.* **642**, 102–106 (2017).
14. Behrendt, G. et al. Dynamic changes in myelin aberrations and oligodendrocyte generation in chronic amyloidosis in mice and men. *Glia* **61**, 273–286 (2013).
15. Keren-Shaul, H. et al. MARS-seq2.0: an experimental and analytical pipeline for indexed sorting combined with single-cell RNA sequencing. *Nat. Protoc.* **14**, 1841–1862 (2019).
16. Jaitin, D. A. et al. Massively parallel single-cell RNA-seq for marker-free decomposition of tissues into cell types. *Science* **343**, 776–779 (2014).
17. Oakley, H. et al. Intraneuronal β-amyloid aggregates, neurodegeneration, and neuron loss in transgenic mice with five familial Alzheimer's disease mutations: potential factors in amyloid plaque formation. *J. Neurosci.* **26**, 10129–10140 (2006).
18. Lake, B. B. et al. Integrative single-cell analysis of transcriptional and epigenetic states in the human adult brain. *Nat. Biotechnol.* **36**, 70–80 (2018).
19. Bost, P. et al. Host–viral infection maps reveal signatures of severe COVID-19 patients. *Cell* **181**, 1475–1488 (2020).
20. Robinson, A. P., Rodgers, J. M., Goings, G. E. & Miller, S. D. Characterization of oligodendroglial populations in mouse demyelinating disease using flow cytometry: clues for MS pathogenesis. *PLoS ONE* **9**, e107649 (2014).
21. Vicuña, L. et al. The serine protease inhibitor SerpinA3N attenuates neuropathic pain by inhibiting T cell-derived leukocyte elastase. *Nat. Med.* **21**, 518–523 (2015).
22. Haile, Y. et al. Granzyme B-inhibitor serpina3n induces neuroprotection in vitro and in vivo. *J. Neuroinflammation* **12**, 157 (2015).
23. Gadani, S. P., Walsh, J. T., Smirnov, I., Zheng, J. & Kipnis, J. The glia-derived alarmin IL-33 orchestrates the immune response and promotes recovery following CNS injury. *Neuron* **85**, 703–709 (2015).

24. Bando, Y. et al. Kallikrein 6 secreted by oligodendrocytes regulates the progression of experimental autoimmune encephalomyelitis. *Glia* **66**, 359–378 (2018).
25. Kwon, O.-C. et al. SGK1 inhibition in glia ameliorates pathologies and symptoms in Parkinson disease animal models. *EMBO Mol. Med.* **13**, e13076 (2021).
26. Gupta, A. & Pulliam, L. Exosomes as mediators of neuroinflammation. *J. Neuroinflammation* **11**, 68 (2014).
27. Pascual, M., Ibáñez, F. & Guerri, C. Exosomes as mediators of neuron–glia communication in neuroinflammation. *Neural Regen. Res.* **15**, 796–801 (2020).
28. Janky, R. et al. iRegulon: from a gene list to a gene regulatory network using large motif and track collections. *PLoS Comput. Biol.* **10**, e1003731 (2014).
29. Hashimoto, R. et al. Origins of oligodendrocytes in the cerebellum, whose development is controlled by the transcription factor, Sox9. *Mech. Dev.* **140**, 25–40 (2016).
30. Stolt, C. C. et al. The Sox9 transcription factor determines glial fate choice in the developing spinal cord. *Genes Dev.* **17**, 1677–1689 (2003).
31. Lee, S.-H. et al. Trem2 restrains the enhancement of tau accumulation and neurodegeneration by β-amyloid pathology. *Neuron* **109**, 1283–1301 (2021).
32. Stine, W. B., Jungbauer, L., Yu, C. & Ladu, M. J. Preparing synthetic Aβ in different aggregation states. *Methods Mol. Biol.* **670**, 13–32 (2011).
33. Constantinescu, C. S., Farooqi, N., O'Brien, K. & Gran, B. Experimental autoimmune encephalomyelitis (EAE) as a model for multiple sclerosis (MS). *Br. J. Pharm.* **164**, 1079 (2011).
34. Rangachari, M. & Kuchroo, V. K. Using EAE to better understand principles of immune function and autoimmune pathology. *J. Autoimmun.* **45**, 31–39 (2013).
35. Falcão, A. M. et al. Disease-specific oligodendrocyte lineage cells arise in multiple sclerosis. *Nat. Med.* **24**, 1837–1844 (2018).
36. Wheeler, M. A. et al. MAFG-driven astrocytes promote CNS inflammation. *Nature* **578**, 593–599 (2020).
37. Dulken, B. W. et al. Single-cell analysis reveals T cell infiltration in old neurogenic niches. *Nature* **571**, 205–210 (2019).
38. Liddelow, S. A. et al. Neurotoxic reactive astrocytes are induced by activated microglia. *Nature* **541**, 481–487 (2017).
39. Hasel, P., Rose, I. V. L., Sadick, J. S., Kim, R. D. & Liddelow, S. A. Neuroinflammatory astrocyte subtypes in the mouse brain. *Nat. Neurosci.* **24**, 1475–1487 (2021). *2021 2410*.
40. Greenwald, N. F. et al. Whole-cell segmentation of tissue images with human-level performance using large-scale data annotation and deep learning. *Nat. Biotechnol.* **40**, 555–565 (2022).
41. Illian, J., Penttinen, A., Stoyan, H. & Stoyan, D. *Statistical Analysis and Modelling of Spatial Point Patterns*. *Statistical Analysis and Modelling of Spatial Point Patterns* (Wiley, 2008).
42. Nagele, R. G. et al. Contribution of glial cells to the development of amyloid plaques in Alzheimer's disease. *Neurobiol. Aging* **25**, 663–674 (2004).
43. Chen, W. T. et al. Spatial transcriptomics and in situ sequencing to study Alzheimer's disease. *Cell* **182**, 976–991 (2020).
44. Serrano-Pozo, A., Betensky, R. A., Frosch, M. P. & Hyman, B. T. Plaque-associated local toxicity increases over the clinical course of Alzheimer disease. *Am. J. Pathol.* **186**, 375–384 (2016).
45. Yin, Z. et al. Immune hyperreactivity of Aβ plaque-associated microglia in Alzheimer's disease. *Neurobiol. Aging* **55**, 115–122 (2017).
46. Griciuc, A. et al. TREM2 acts downstream of CD33 in modulating microglial pathology in Alzheimer's disease. *Neuron* **103**, 820–835 (2019).
47. Rajala, T., Murrell, D. J. & Olhede, S. C. Detecting multivariate interactions in spatial point patterns with Gibbs models and variable selection. *J. R. Stat. Soc. Ser. C. Appl. Stat.* **67**, 1237–1273 (2018).
48. Mathys, H. et al. Single-cell transcriptomic analysis of Alzheimer's disease. *Nature* **570**, 332–337 (2019).
49. Thrupp, N. et al. Single-nucleus RNA-seq is not suitable for detection of microglial activation genes in humans. *Cell Rep.* **32**, 108189 (2020).
50. Chen, S. et al. Spatially resolved transcriptomics reveals unique gene signatures associated with human temporal cortical architecture and Alzheimer's pathology. Preprint at https://www.biorxiv.org/content/10.1101/2021.07.07.451554v1 (2021).
51. Bin, J. M., Harris, S. N. & Kennedy, T. E. The oligodendrocyte-specific antibody 'CC1' binds Quaking 7. *J. Neurochem.* **139**, 181–186 (2016).
52. Venegas, C. & Heneka, M. T. Danger-associated molecular patterns in Alzheimer's disease. *J. Leukoc. Biol.* **101**, 87–98 (2017).
53. Zhang, P. et al. Senolytic therapy alleviates Aβ-associated oligodendrocyte progenitor cell senescence and cognitive deficits in an Alzheimer's disease model. *Nat. Neurosci.* **22**, 719–728 (2019).
54. Zamanian, J. L. et al. Genomic analysis of reactive astrogliosis. *J. Neurosci.* **32**, 6391–6410 (2012).
55. Deczkowska, A. et al. Mef2C restrains microglial inflammatory response and is lost in brain ageing in an IFN-I-dependent manner. *Nat. Commun.* **8**, 717 (2017).
56. Subramanian, A. et al. Gene set enrichment analysis: a knowledge-based approach for interpreting genome-wide expression profiles. *Proc. Natl Acad. Sci. USA* **102**, 15545–15550 (2005).

Methods

Mice. Heterozygous 5xFAD transgenic mice (on a C57/BL6-SJL background) that overexpress familial AD mutant forms of human APP (the Swedish mutation, K670N/M671L; the Florida mutation, I716V; and the London mutation, V717I) and PS1 (M146L/L286V) transgenes under the transcriptional control of the neuron-specific mouse Thy-1 promoter[17] (5XFAD line Tg6799, Jackson Laboratory) were taken throughout adulthood in different timepoints as indicated in the text. Genotyping was performed by polymerase chain reaction (PCR) analysis of tail DNA. Throughout the study, WT controls in each experiment were non-transgene littermates from the relevant mouse colonies. Mice were bred and maintained by the animal breeding center of the Weizmann Institute of Science. All experiments detailed herein complied with the regulations formulated by the Institutional Animal Care and Use Committee of the Weizmann Institute of Science.

Brain dissociation for single-cell suspension. Mice were euthanized using an overdose of ketamine–xylazine, followed by transcardial perfusion with cold PBS, and whole brains were excised. Tissues were chopped into small pieces and subjected to 30 minutes of enzymatic digestion using papain (Worthington, LS003127) at 37 °C, followed by manual trituration using a 5-ml pipette and filtering through a 70-µm cell strainer. Cells were pelleted at 800*g* for 5 minutes at 4 °C and then suspended in ovomucoid protease inhibitor (Worthington, LS003086) solution to stop papain activity. Cells were pelleted again at 600*g* for 5 minutes at 4 °C and washed, and myelin debris was removed by 30% Percoll gradient (GE Healthcare, 17–0891–01). Then, cells were pelleted and washed again and subjected to 20 minutes of Fc block (1:200) followed by 30 minutes of cell surface staining. Immediately before fluorescence-activated cell sorting (FACS), cells were washed, filtered through a 70-µm cell strainer and suspended in sorting buffer (PBS supplemented with 0.2 mM EDTA pH 8 and 0.5% BSA), and DAPI was added. Samples were kept on ice at all times except for enzymatic digestion.

Single-cell sorting. Cell populations were sorted using FACSAriaIII or FACSymphony-S6 and FACSDiva software (BD Biosciences). For the sorting of all the non-immune populations, samples were gated for $CD45^-$ (APC, clone 30F-11, 17-0451-82, eBioscience, or 103115, BioLegend, 1:200) while excluding debris (FSC-A versus SSC-A), dead cells ($DAPI^+$) and doublets (FSC-A versus FSC-H). To enrich for different cell populations, the following markers were used: GalC (oligodendrocytes, FITC, clone mGalC, FCMAB312F, Milli-Mark, 1:10) and Ly6A/E (endothelial, BV605, clone D7, 108133, BioLegend, 1:150). Isolated cells were single-cell sorted into 384-well cell capture plates containing 2 µl of lysis solution and barcoded poly(T) reverse transcription (RT) primers for scRNA-seq[15]. Four empty wells were kept in each 384-well plate as a no-cell control. Immediately after sorting, each plate was spun down to ensure cell immersion into the lysis solution, snap-frozen on dry ice and stored at −80 °C until processing. To record the marker level of each single cell, the FACSDiva 'index sorting' function was activated during single-cell sorting. After the sequencing and analysis of the single cells, each surface marker was linked to the genome-wide expression profile. This methodology was used to optimize the gating strategy and to eliminate autofluorescent cells. No statistical methods were used to predetermine sample sizes, but our sample sizes are similar to or greater than those reported in previous publications[9,10].

Single-cell RNA library preparation by MARS-seq. Single-cell libraries were prepared using the MARS-seq 2.0 protocol[15]. In brief, mRNA from the cells sorted into cell capture plates were barcoded, converted into cDNA and pooled. The pooled sample was linearly amplified by T7 in vitro transcription. The resulting RNA was fragmented and converted into a sequencing-ready library by tagging the samples with pool barcodes and Illumina sequences during ligation, RT and PCR. Each pool of cells was tested for library quality as described in the MARS-seq 2.0 protocol.

Low-level processing of the scRNA-seq data. MARS-seq libraries, pooled at equimolar concentrations, were sequenced using an Illumina NextSeq 500 or NovaSeq 6000 sequencer at a sequencing depth of 20,000–50,000 reads per cell. Reads were condensed into original molecules by counting the same unique molecular identifiers (UMIs). Statistics on empty-well spurious UMI detection were used to ensure that the batches used for analysis showed a low level of cross-single-cell contamination (<3%). Mapping of reads was done using HISAT (version 0.1.15)[57]; reads with multiple mapping positions were excluded. Reads were associated with genes if they were mapped to an exon, using the UCSC Genome Browser for reference. Exons of different genes that shared genomic positions on the same strand were considered a single gene with a concatenated gene symbol.

Basic statistical analysis and visualization. Most of the variables investigaed in our study are not normally distributed; thus, the Kruskal–Wallis rank test was used to compare values between groups. As the Kruskall–Wallis test is a non-parametric one, data normality does not have to be checked. Ordinary least square regressions were computed using the lm() function, and the *P* value associated with slope was computed using the summary() function. Quality of the linear models was visually checked for any possible bias. Correction for multiple testing was done using Benjamini–Hochberg correction implemented in the p.adjust() function when necessary.

For visualization, when the number of points per group was greater than 30, the boxplot() function was used with parameters set to default except for the 'outline' parameter, which was set to FALSE.

scRNA-seq data processing and clustering. scRNA-seq expression data analysis was performed using the R-based Pagoda2 pipeline (https://github.com/hms-dbmi/pagoda2/)[18] in addition to an in-house R script. Low-quality cells were removed using the following strategy. Cells with fewer than 350 UMIs and more than 30% of mitochondrial genes were removed. The number of highly variables genes (HVGs) was determined using the adjustVariance() function with the gam parameter set to 5. HVGs were selected using the following strategy. For each gene, its number of zeros and its mean expression were computed. A local polynomial model was then used to predict the number of zeros according to the log mean expression (LOESS function with degree parameter set to 2). The residuals of this model (excess of zeros) were then used to rank the genes, and the genes with the highest excess of the zeros were considered the most HVGs. Principal component analysis (PCA) reduction was then computed using the calculatePcaReduction() function. The number of computed principal components (PCs) was changed in each analysis due to a variable number of cells and cellular heterogeneity. A *k*-nearest neighbor graph was then built with the function makeKnnGraph() with the *k* value set to 30 and the distance parameter set to 'cosine'. Clusters were computed using the Louvain clustering approach implemented in the getKnnClusters() and multilevel.community() functions. Marker genes were identified using the getDifferentialGenes() function. UMAP low-dimensional embedding was computed using the uwot R package and, more precisely, the umap() function with the n_neighbors parameter set to 30 and the metric parameter set to 'cosine'. To group clusters of cells in the first round of analysis, mean gene expression of the most variable genes was computed using the aggregate() function. Spearman's correlation matrix was computed using the cor() function with the method parameter set to 'Spearman'. Hierarchical clustering was then performed on this matrix using Ward's method, and the resulting tree was used to aggregate the cell clusters. Data collection and analysis were not performed blinded to the conditions of the experiments.

Single-cell differential gene expression analysis and power analysis. To perform differential expression analysis, a dichotomized-based approach was used as previously described[19]. In brief, gene expression was first dichotomized (if the normalized expression was greater than 0, the gene was considered as expressed), and then a binomial generalized linear model (GLM) was computed with a complementary log–log link function (cloglog) using the glm() R function. To mitigate the effect of library size variation across the cells, it was included as a covariate in the model. The corresponding *P* values were computed using a likelihood ratio test (LRT) and then corrected using Benjamini–Hochberg correction.

Power analysis was performed by randomly sampling 15 times a given proportion of the oligodendrocytes (80%, 70%, 60%, 50%, 20%, 10% and 5%) and then performing the dichotomized gene expression analysis described above.

Poisson regression for the analysis of cluster abundancy. Robust detection of cell clusters that were differentially abundant between WT and 5xFAD mice was performed for oligodendrocyte clusters using a Poisson regression where the observed variable is the number of oligodendrocytes belonging to this cluster in each mouse, and the explanatory variables are the total number of cells sequenced from each mouse and the genotype of the mouse (5xFAD or WT). This model was fitted using the glm() R core function. An exponential link function was used, and the total number of cells was, therefore, logged. *P* values were corrected using Benjamini–Hochberg correction, implemented in the p.adjust() function.

Promoter motif analysis. Promoter analysis was performed using iRegulon[28] (Cytoscape plugin, version 1.3). The 'Species and gene nomenclature' parameter was set to 'Mus musculus, MGI symbols', and only motifs 500 base pairs upstream of the transcription start sites were used. All other parameters were set to default values.

GSEA. GSEA was performed using the liger (version 1.12) and gskb (version 1.16)[58] packages. In brief, a gene set describing a list of biological pathways was loaded (mm_pathway object) from the gskb library and then used to analyze the $\log_2$FC value list using the bulk.gsea() function from liger.

Meta-analysis of previously published scRNA-seq. The dataset containing the P301L and the PS2/APP/P301L and the two EAE datasets used in the meta-analysis were downloaded from the Gene Expression Omnibus (GEO) server by the following accession numbers: P301L and the PS2/APP/P301L: GSE153895; acute EAE: GSE113973; and multi-phasic EAE: GSE118257. Annotations of the samples were done using the getGEO() function from the GEOquery package (version 2.48). The aging SVZ 10x scRNA-seq data were kindly provided by the authors. Expression data were processed using the same approach as described above.

A cell cluster was considered corresponding to oligodendrocytes if it specifically expressed a known oligodendrocyte marker, such as Plp1 or Mbp.

Primary oligodendrocyte cultures. Primary OPCs were cultured as follows: P0–P3 mouse pups were decapitated, and cortices were extracted and put in DMEM media with penicillin–streptomycin on ice. Then, cortices were homogenized by two triturations with a 19-gauge needle, followed by two triturations with a 21-gauge needle. Then, the suspension was centrifuged (200*g*, 5 minutes, room temperature), suspended in glia medium (DMEM, 10% heat-inactivated FBS, 5% heat-inactivated horse serum, penicillin–streptomycin) and seeded in flasks. Glia medium was replaced every 3 days, and, from the sixth day, insulin (5 µl ml^{-1}, Sigma-Aldrich, l6634) was supplied. After 10 days, flasks were gently knocked, and media were removed to remove microglia, followed by shaking overnight at 250 r.p.m. at 37 °C. The next day, OPCs were purified from the supernatant using MACS separation O4 beads (130-096-670, Miltenyi Biotec) and seeded over poly-D-lysine, poly-L-ornithine pre-coated plates. OPCs were grown in DMEM supplemented with horse serum, B-27, pyruvate, penicillin–streptomycin, GlutaMAX, T3 and T4. Media were replaced every 2 days.

Culture stimulation, bulk RNA purification and library preparation. Oligodendrocytes were stimulated upon maturation. For Aβ stimulation, different aggregation states were prepared from HFIP-treated $A\beta_{1-42}$ (Bachem, 4090148) as previously described[32]. Scrambled Aβ was used as control (Bachem, 4064853). Cells were treated with aggregated Aβ at 20 nM concentration for 24 hours. Cells were collected, and mRNA was purified using Dynabeads mRNA Purification Kit (Invitrogen). Libraries were prepared using a modified MARS-seq protocol for bulk.

Analysis of bulk RNA-seq data. Bulk sequencing data were analyzed using the DESeq2 (version 1.24)[59] and apeglm (version 1.60)[60] packages. Samples with fewer than 2×10^5 UMIs sequenced and genes with fewer than 50 total UMIs were removed from the analysis. A DESeq2 object was created using the dds() function. The underlying statistical model was fit using the DESeq() function with parameter 'fitType' set to 'parametric'. Owing to the low number of technical replicates used in each experiment (three samples per condition), the shrank $\log_2$FCs were computed using the lfcShrink function with the parameter 'type' set to 'apeglm'.

Immunofluorescence and imaging. For mouse immunofluorescence, mice were euthanized and intracardially perfused with PBS, and brains were extracted and fixed in paraformaldehyde 2.5% overnight and then washed with PBS and immersed in 30% sucrose until sinking. Then, 30-µm free-floating brain sections were cut using a sliding microtome (Leica) and quenched using 100 mM NH_4Cl for one hour at room temperature, blocked in PBS with 10% donkey serum and 0.5% Triton and then stained using the following primary antibodies: Olig2 (AB9610, Merck, 1:200), Serpina3n (AF4709, R&D Systems, 1:200) and hAβ (BLG-803001, BioLegend, 1:200) in PBS with 5% donkey serum and 0.1% Triton. Secondary antibodies used were donkey anti-rabbit cy2 (Jackson ImmunoResearch, 711-225-152, 1:200), donkey anti-goat cy3 (Jackson ImmunoResearch, 705-165-147, 1:200) and donkey anti-mouse cy5 (Jackson ImmunoResearch, 715-175-151, 1:200). For human immunofluorescence, paraffin-embedded human brain temporal cortex sections of postmortem AD and non-demented, aged-matched individuals were obtained from the Oxford Brain Bank (formerly known as the Thomas Willis Oxford Brain Collection) with appropriate consent and ethics committee approval by the Weizmann Institutional Review Board. After de-paraffinization, antigen retrieval was performed in Tris-EDTA (pH 9). Sudan black (0.1%) treatment was performed before staining to reduce autofluorescence. Aβ staining was done by thioflavin-S (1%), followed by primary antibodies CC1 (ab16794, Abcam, 1:50) and SERPINA3 (ab205198, Abcam, 1:100). Secondary antibodies used were donkey anti-rabbit cy5 (Jackson ImmunoResearch, 711-175-152, 1:200) and donkey anti-mouse cy3 (Jackson ImmunoResearch, 715-165-150, 1:200). Representative images were captured using a confocal microscope (LSM 880, ×20 and ×63 lens), and Zeiss ZEN software was used for image capturing. Representative images were merged and optimized using Adobe Photoshop. For DOL quantification (human and mouse) and plaque association (mouse), an Olympus BX61VS slide scanner and VA-ASW-S6 software were used. For oligodendrocyte culture bright-field imaging, an Olympus IC70 microscope with an XM10 CCD camera was used.

Image processing. Analysis was conducted on raw images. All image processing steps (segmentation and quantification) were performed using Python version 3.9 in a Jupyter Notebook. Cells were first segmented using the Mesmer tool from the Python DeepCell package[40]. The nuclear segmentation mode was used (im. compartment='nuclear') on the DAPI channel, and the resulting masks were extended using the expand_labels() function from the skimage package using a 5-pixel radius disk as a mask. To identify the plaques, a Laplacian of Gaussian transform was applied to the Aβ channel by first applying a Gaussian filter of size 50 (Gaussian function from the skimage package) and then applying a discrete Laplacian filter (Laplace function). The resulting image was thresholded using Otsu's automated thresholding, implemented by the threshold_otsu() from the skimage package, and watershed segmentation was used. In brief, a distance map was computed from the binary image using the distance_transform_edt() function from the scipy package, and local peaks were extracted with the corner_peaks() function from the skimage package with the following parameter values: footprint = np.ones((10,10)), min_distance = 20 and exclude_border = False. The final step of the watershed was then performed using the watershed() function from skimage. The various properties of the identified cells and plaques (size, location and mean marker expression) were computed using the regionprops_table() function from the skimage package and then exported as a text file.

Spatial analysis. The analysis of the resulting image segmentation/processing steps was solely performed on R 4.0.3. Automated thresholding of the fluorescence intensity was performed using Otsu's thresholding method, implemented by an in-house script. As the intensity distribution was highly heavy-tailed for the human samples, a cubic root transform was applied to get a more 'normal-like' distribution before performing the thresholding. Normalized Besag's L functions were computed using the Linhom() function from the Spatstat package. To get the normalized version of this function, the theoretical value of the function was subtracted from the estimated value.

To fit the penalized Gibbs model, the PenGe package was used (https://github.com/antiphon/PenGE). First, a spatstat object was built using the ppp() function with a default window of width 20,000 and height 6,500. The model was fitted using the make_Q_stepper_multi() and fitGlbin_CV() functions. Thirty different values on a log-scale of lambda were used, and the vector of the range was set to c(100,250,500,1000,1500) (pixel scale with 3 pixels equal to 1 µm). The lambda with the highest log-likelihood was selected, and the corresponding model was used for analysis.

Human spatial transcriptomic pre-processing. BCL files were processed with SpaceRanger (version 1.2.2) to generate FASTQ files via spaceranger mkfastq. The FASTQ file was then aligned and quantified based on the reference GRCh38 Reference-2020-A via spaceranger count. The functions spaceranger mkfastq and spaceranger count were used for demultiplexing sample and transcriptome alignment via the default parameter settings. Sctransform[61] (version 0.3.2) was used to normalize the raw count data for the following analysis based on default parameters.

Spatial transcriptomic data analysis. Spatial transcriptomic data were processed using the following approach. First, low-quality spots having fewer than 1,000 UMIs were filtered out. Using the Pagoda2 pipeline, the 1,000 most variable genes were selected using the r$adjustVariance() function. Then, using the CountClust package, a latent Dirichlet allocation (LDA) analysis was performed (FitGoM() function) using five different numbers of topics (10, 15, 20, 25 and 30 topics) and with the 'tolerance' parameter set to 100. The model displaying the lowest Bayesian information criterion (BIC) score was selected and used for further analysis.

To identify biologically meaningful genes, the contribution table obtained from the FitGoM function was normalized by applying the following transformation to the contribution *cij* of each gene *i* and for each topic *j*:

$$cij' = \lambda^* log\,(cij) + (1 - \lambda)^* log\,(cij/Si)$$

where '*cij*' is the normalized contribution of gene *i* for topic *j*; ƛ is a parameter set to 0.5; and *Si* is the contribution of gene *i* to the total number of UMIs.

Reporting summary. Further information on research design is available in the Nature Research Reporting Summary linked to this article.

Data availability

Raw and processed mouse sequencing data that support the findings of this study have been deposited in the Gene Expression Omnibus database under accession number GSE202297.

Code availability

All the code is available on GitHub at: https://github.com/PierreBSC/DOL_project

References

57. Kim, D., Langmead, B. & Salzberg, S. L. HISAT: a fast spliced aligner with low memory requirements. *Nat. Methods* **12**, 357–360 (2015).
58. Lai, L. et al. GSKB: a gene set database for pathway analysis in mouse. Preprint at https://www.biorxiv.org/content/10.1101/082511v1.full (2016).
59. Love, M. I., Huber, W. & Anders, S. Moderated estimation of fold change and dispersion for RNA-seq data with DESeq2. *Genome Biol.* **15**, 550 (2014).
60. Zhu, A., Ibrahim, J. G. & Love, M. I. Heavy-tailed prior distributions for sequence count data: removing the noise and preserving large differences. *Bioinformatics* **35**, 2084–2092 (2019).
61. Hafemeister, C. & Satija, R. Normalization and variance stabilization of single-cell RNA-seq data using regularized negative binomial regression. *Genome Biol.* **20**, 296 (2019).

Acknowledgements

The research of I.A. is supported by the Seed Networks for the Human Cell Atlas of the Chan Zuckerberg Initiative, the Thompson Family Foundation Alzheimer's Research Fund and the Adelis Foundation. I.A. is an Eden and Steven Romick Professorial Chair, supported by the HHMI International Scholar Award, a European Research Council Consolidator Grant (724471-HemTree2.0), an MRA Established Investigator Award (509044), the DFG (SFB/TRR167), the Ernest and Bonnie Beutler Research Program for Excellence in Genomic Medicine, the Helen and Martin Kimmel awards for innovative investigation and the SCA award of the Wolfson Foundation and Family Charitable Trust. Research in the M.S. laboratory is supported by Advanced European Research Council grants (741744); Israel Science Foundation (ISF) research grant 991/16; and ISF-Legacy Heritage Bio-Medical Science Partnership research grant 1354/15. We would like to thank the Adelis and Thompson Foundations for their generous support of our AD research. This work is also supported by awards K01-AG056673 and R56-066782–01 from the National Institute on Aging of the National Institutes of Health, R01-GM131399 (Q.M.) from the National Institute of General Medical Sciences, AARF-17–505009 (H.F.) from the Alzheimer's Association and W81XWH1910309 (H.F.) from the US Department of Defense.

Author contributions

M.S., I.A. and M.K. conceived the study. M.K and P.B. designed the experiments. M.K. conducted the animal work, isolated cells and generated single-cell sequencing libraries. M.K. and S.H. conducted the imaging experiments. M.K. and S.H. conducted the in vitro experiments, with assistance from R.H. P.B. conducted the data analysis for the sequencing, re-analysis of the published datasets and spatial analysis of the mouse LPS treatment Visium data. P.B. developed a new algorithmic approach for image analysis and analyzed imaging experiments. Y.C., S.C, Q.M. and H.F. conducted the Visium spatial transcriptomics on human brain samples and the data analysis. B.S. and B.B. provided the computational resources for analysis. M.K., M.S., P.B. and I.A. wrote the paper, with input from all the other authors.

Competing interests

M.S. serves as a consultant of Immunobrain Checkpoint Ltd.

Additional information

Extended data is available for this paper at https://doi.org/10.1038/s41593-022-01104-7.

Supplementary information The online version contains supplementary material available at https://doi.org/10.1038/s41593-022-01104-7.

Correspondence and requests for materials should be addressed to Michal Schwartz or Ido Amit.

Peer review information *Nature Neuroscience* thanks Sarah Jäkel and the other, anonymous, reviewer(s) for their contribution to the peer review of this work.

Reprints and permissions information is available at www.nature.com/reprints.

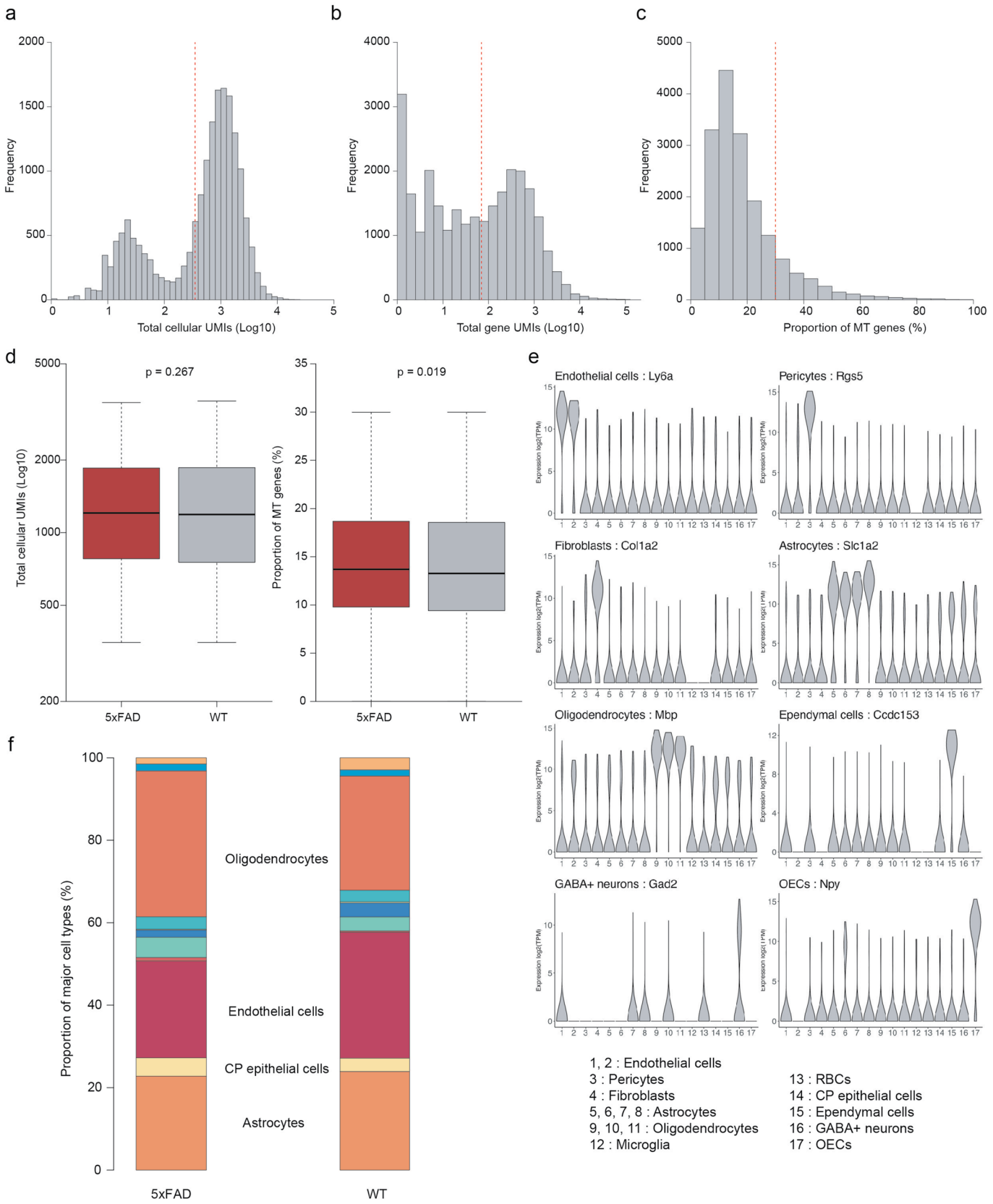

Extended Data Fig. 1 | See next page for caption.

Extended Data Fig. 1 | Quality control of CD45− libraries described in Fig. 1. Extended data Fig. 1 associated to Fig. 1. (**a**) Distribution of total cellular unique molecular identifiers (UMI). Dashed line marks the threshold for analysis. (**b**) Distribution of total gene UMIs. Dashed line marks the threshold for analysis. (**c**) Distribution of the proportion of mitochondrial genes. Dashed line marks the threshold for analysis. (**d**) Comparison of the total cellular UMI distribution in cells from 5xFAD and WT mice (left panel) and the proportion of mitochondrial genes in cells from 5xAD and WT mice (right panel). *P* values were computed using a Kruskal-Wallis test. The box bounds the IQR. Line, median. Whiskers extend to a maximum of 1.5*IQR beyond the box. n = 18 independent mice (9 5xFAD, 9 WT) (**e**) Violin plot of known marker genes expression across the different cell clusters. (**f**) Comparison of the main cell-type proportions between 5xAD and WT mice.

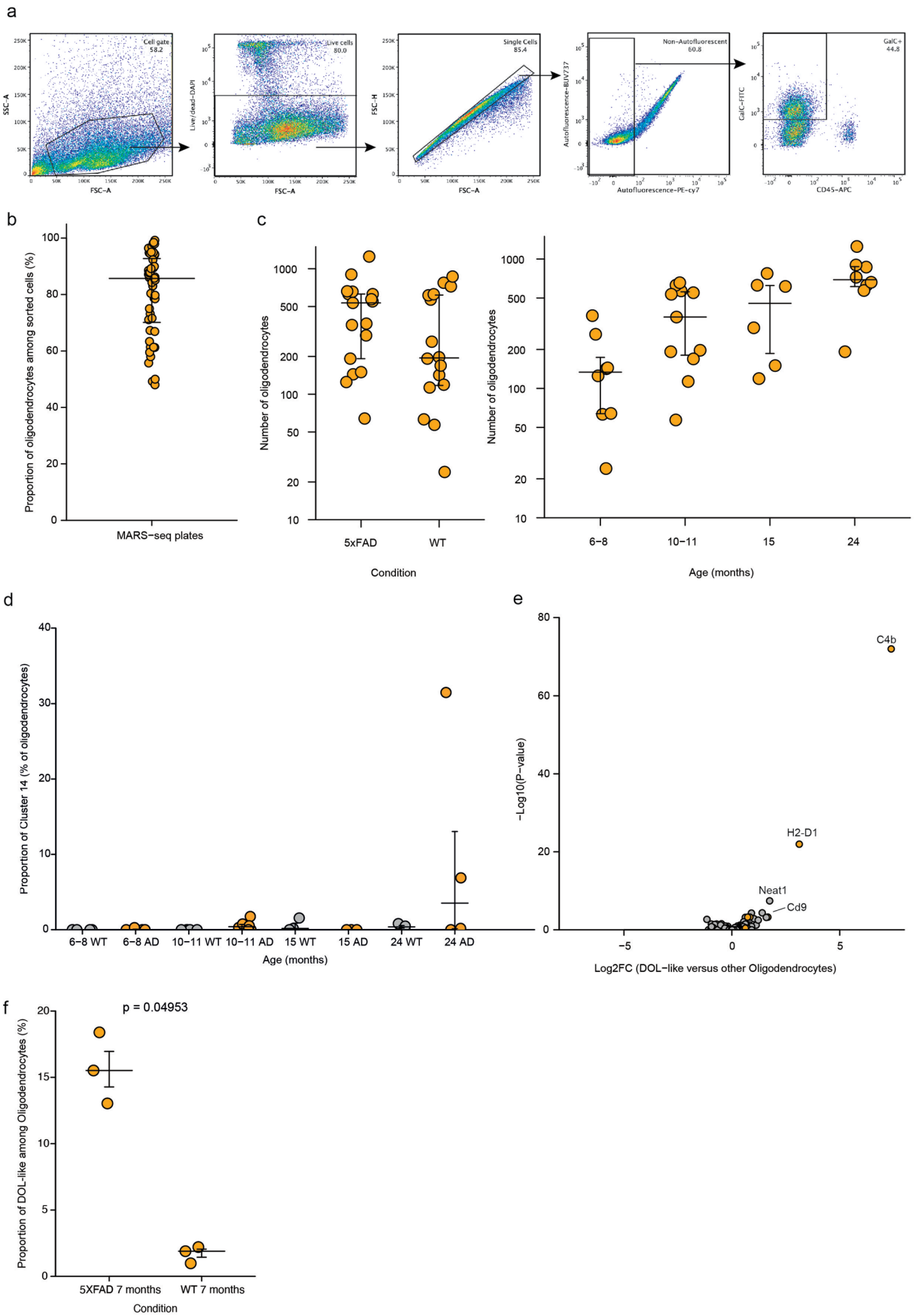

Extended Data Fig. 2 | See next page for caption.

Extended Data Fig. 2 | Quality control of GalC+ libraries described in Fig. 2. Extended data Fig. 2 associated to Fig. 2. (**a**) Gating strategy used to enrich for oligodendrocytes. (**b**) Proportion of oligodendrocytes isolated in each sequenced plate. Large bars correspond to the median and small bars to IQR. n = 48 384-well plates (**c**) Number of oligodendrocytes sequenced for each 5xAD and WT mice (left panel) and across ages (right panel). Large bars correspond to the median and small bars to IQR. n = 33 independent mice (17 5xFAD, 16 WT) (**d**) Proportion of cluster 14 in WT and 5xFAD mice across ages. Large bars correspond to the median and small bars to IQR. n = 33 independent mice (across ages: 6–8 m; n = 4 5xFAD, 4 WT, 10–11 m; n = 6 5xFAD, 5 WT, 15 m; n = 3 5xFAD, 3 WT, 24 m; n = 4 5xFAD, 4 WT) (**e**) Volcano plot corresponding to the differential expression analysis between DOL-like and the rest of oligodendrocytes as identified by Zhou et al.11. DOL genes are colored in orange. (**f**) Proportion of DOL-like among oligodendrocytes between 5xFAD and WT mice in the data by Zhou et al.11. P-value was computed using the Kruskal-Wallis test.

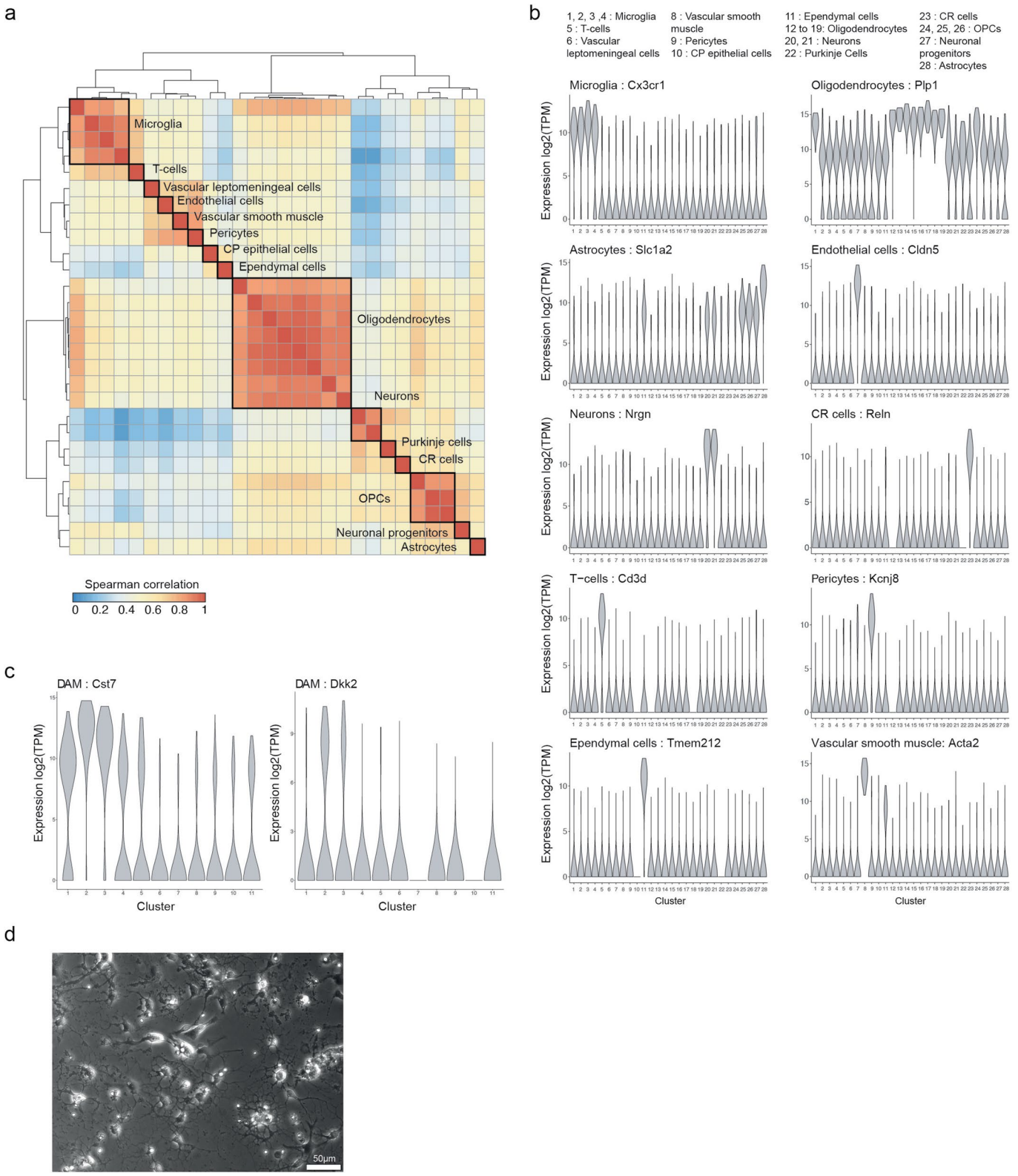

Extended Data Fig. 3 | Cell type annotation of dataset described in Fig. 3 and culture quality control. Extended data Fig. 3 associated to Fig. 3. (**a**) Spearman correlation between the mean transcriptomic profiles of the cell clusters identified in the dataset from Lee et al. (**b**) Violin plot of known marker genes across the different cell clusters. (**c**) Violin plot of known DAM marker gene expression across the different microglia clusters after refined clustering. (**d**) Representative bright-field microscopy image of the primary oligodendrocyte culture; scale bar corresponds to 50 µm. Representative results from 12 independent experiments.

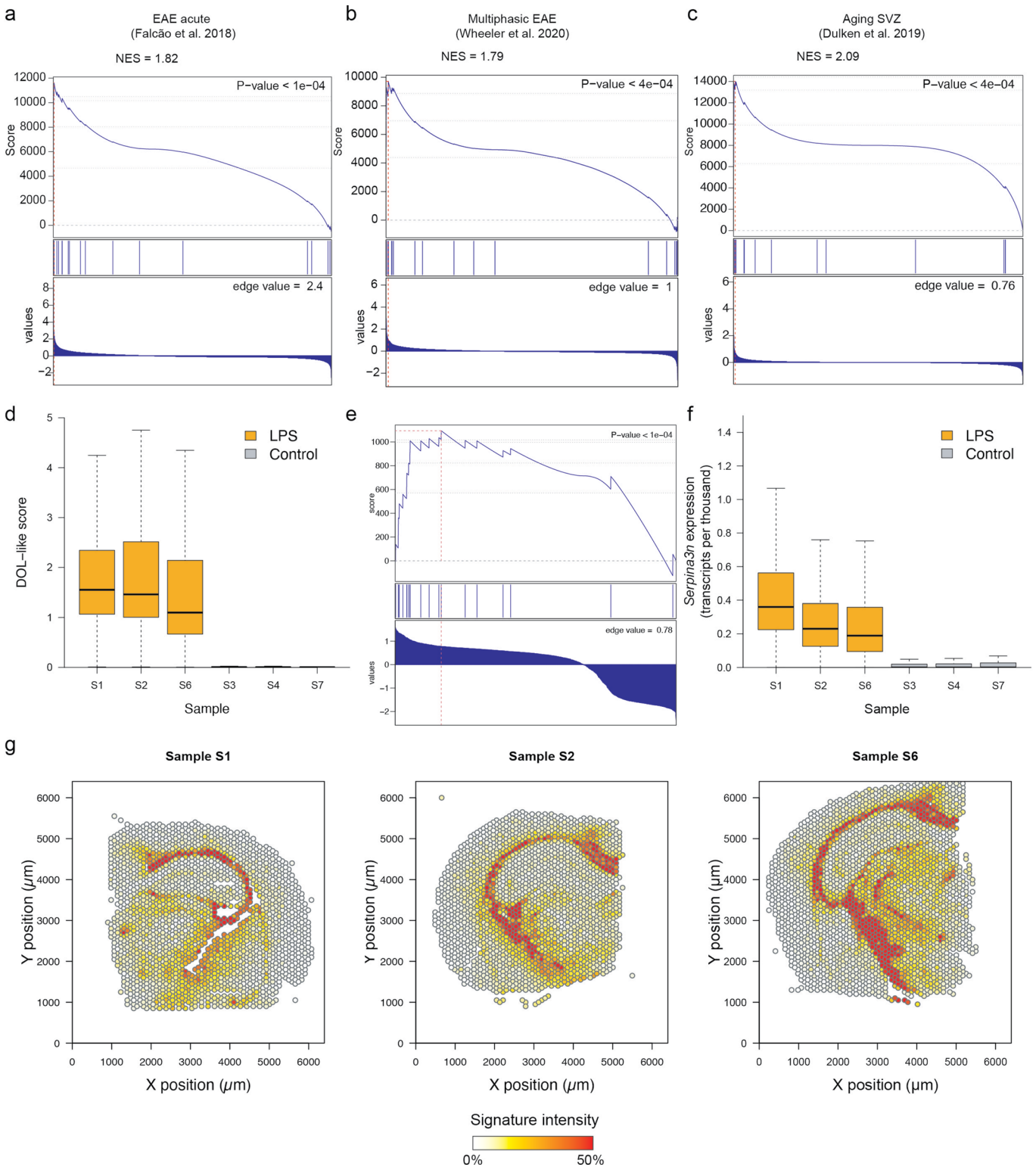

Extended Data Fig. 4 | GSEA and quality control of datasets described in Fig. 4. Extended data Fig. 4 **associated to** Fig. 4**. (a)** GSEA analysis plot corresponding to the acute EAE dataset. **(b)** GSEA analysis plot corresponding to the multiphasic EAE dataset. **(c)** GSEA analysis plot corresponding to the aging SVZ dataset. **(d)** score of topic number 8, corresponding to DOL-like signature, in LPS-stimulated and control samples. n = 6 independent samples (3 LPS-stimulated, 3 control). Thick line corresponds to the median, the bottom and upper limits of the box to the first and third quartile, respectively. The lower and upper whiskers correspond to the lowest and highest values respectively within the range of the first (third) quartile minus (plus) 1.5 times the Interquartile range. **(e)** GSEA analysis plot of the DOL signature in topic 8. **(f)** *Serpina3n* expression (transcripts per thousand) in LPS-treated and control mice. n = 6 independent samples (3 LPS-stimulated, 3 control). p-value was computed by performing a Gene Set Enrichment Analysis as described by Subramanian et al[56]. Thick line corresponds to the median, the bottom and upper limits of the box to the first and third quartile, respectively. The lower and upper whiskers correspond to the lowest and highest values respectively within the range of the first (third) quartile minus (plus) 1.5 times the Interquartile range. **(g)** Intensity of the oligodendrocyte signature across the sections of the three LPS treated mice.

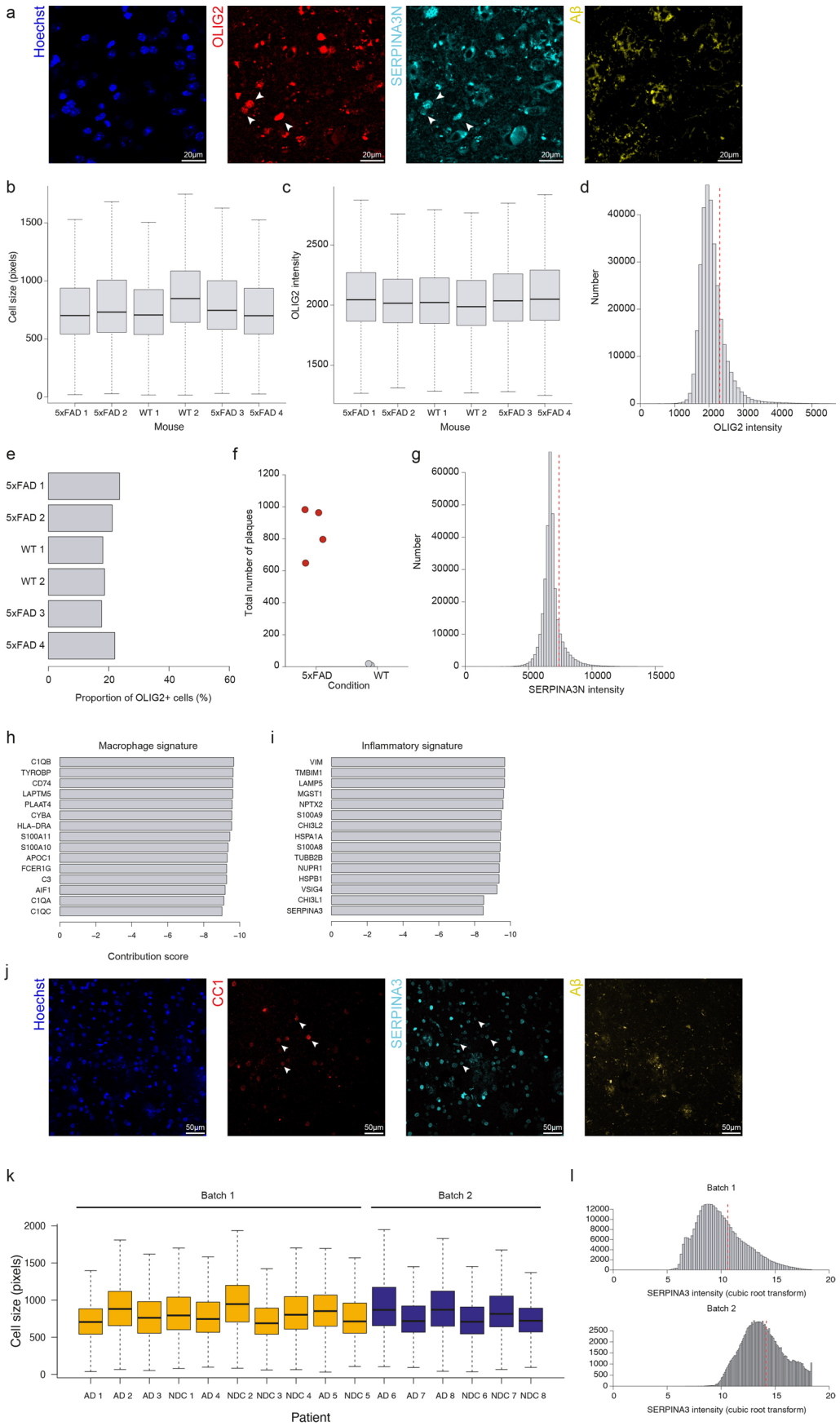

Extended Data Fig. 5 | See next page for caption.

Extended Data Fig. 5 | Quality control of image analysis described in Fig. 5. Extended data Fig. 5 associated to Fig. 5**. (a)** Separated channels corresponding to the 5xFAD brain sample in Fig. 5a; scale bar corresponds to 20 μm. **(b)** Distribution of cell size across mice samples. The box bounds the IQR. Line, median. Whiskers extend to a maximum of 1.5*IQR beyond the box. n = 6 independent samples (4 5xFAD, 2 WT). **(c)** Distribution of OLIG2 intensity across mouse samples. The box bounds the IQR. Line, median. Whiskers extend to a maximum of 1.5*IQR beyond the box. n = 6 independent samples (4 5xFAD, 2 WT). **(d)** Distribution of OLIG2 intensity and estimated threshold (vertical red line). **(e)** Proportion of OLIG2+ cells across mouse samples. **(f)** Number of plaques in 5xFAD (n = 4) and WT (n = 2) mice. **(g)** Distribution of SERPINA3N intensity and the estimated threshold (vertical red line). **(h)** The 15 most contributing genes to the macrophage signature. **(i)** The 15 most contributing genes to the inflammatory signature. **(j)** Separated channels corresponding to the postmortem AD brain sample in Fig. 5i; scale bar corresponds to 50 μm. **(k)** Distribution of cell size across human samples. The box bounds the IQR. Line, median. Whiskers extend to a maximum of 1.5*IQR beyond the box. n = 16 independent samples (8 AD, 8 NDC). **(l)** Distribution of SERPINA3 intensity and the estimated threshold (vertical red line) for the two different batches of samples.

nature portfolio

Corresponding author(s): Michal Schwartz, Ido Amit

Last updated by author(s): 2022/05/09

Reporting Summary

Nature Portfolio wishes to improve the reproducibility of the work that we publish. This form provides structure for consistency and transparency in reporting. For further information on Nature Portfolio policies, see our Editorial Policies and the Editorial Policy Checklist.

Statistics

For all statistical analyses, confirm that the following items are present in the figure legend, table legend, main text, or Methods section.

n/a	Confirmed
☐	☒ The exact sample size (*n*) for each experimental group/condition, given as a discrete number and unit of measurement
☒	☐ A statement on whether measurements were taken from distinct samples or whether the same sample was measured repeatedly
☐	☒ The statistical test(s) used AND whether they are one- or two-sided *Only common tests should be described solely by name; describe more complex techniques in the Methods section.*
☐	☒ A description of all covariates tested
☐	☒ A description of any assumptions or corrections, such as tests of normality and adjustment for multiple comparisons
☒	☐ A full description of the statistical parameters including central tendency (e.g. means) or other basic estimates (e.g. regression coefficient) AND variation (e.g. standard deviation) or associated estimates of uncertainty (e.g. confidence intervals)
☐	☒ For null hypothesis testing, the test statistic (e.g. *F*, *t*, *r*) with confidence intervals, effect sizes, degrees of freedom and *P* value noted *Give P values as exact values whenever suitable.*
☒	☐ For Bayesian analysis, information on the choice of priors and Markov chain Monte Carlo settings
☒	☐ For hierarchical and complex designs, identification of the appropriate level for tests and full reporting of outcomes
☒	☐ Estimates of effect sizes (e.g. Cohen's *d*, Pearson's *r*), indicating how they were calculated

Our web collection on statistics for biologists contains articles on many of the points above.

Software and code

Policy information about availability of computer code

Data collection	FACS DIVA software v8.0 (BD Biosciences, San Jose, CA) used to sort the cells. Immunofluorescence imaging was done using Zeiss ZEN software. Slide scanning was done using VA-ASW-S6 software
Data analysis	All statistical analysis were done using R version 4.0.3 Analysis of scRNA-seq data were performed using two R packages : Pagoda2 (version 1.0.0) and uwot (0.1.10). Differential expression analysis was performed using an in-house code already described (Bost et al. Cell 2020, github.com/PierreBSC/Verona_COVID19/blob/master/ScRNA_seq_Verona_cohort_script.R). Spatial analysis were done using the following two R packages : spatstat (1.64) and PenGE (0.2.2,) Image processing was done using Python 3.9 and the two following Python packages : DeepCell (0.9.0) and scikit-image (0.18.0) All scripts used for the analysis are available at : https://github.com/PierreBSC/DOL_project .

For manuscripts utilizing custom algorithms or software that are central to the research but not yet described in published literature, software must be made available to editors and reviewers. We strongly encourage code deposition in a community repository (e.g. GitHub). See the Nature Portfolio guidelines for submitting code & software for further information.

Data

Policy information about availability of data

All manuscripts must include a data availability statement. This statement should provide the following information, where applicable:

- Accession codes, unique identifiers, or web links for publicly available datasets
- A description of any restrictions on data availability
- For clinical datasets or third party data, please ensure that the statement adheres to our policy

Raw and processed data are fully available on GEO plateform with the accession number GSE202297

Field-specific reporting

Please select the one below that is the best fit for your research. If you are not sure, read the appropriate sections before making your selection.

☒ Life sciences ☐ Behavioural & social sciences ☐ Ecological, evolutionary & environmental sciences

For a reference copy of the document with all sections, see nature.com/documents/nr-reporting-summary-flat.pdf

Life sciences study design

All studies must disclose on these points even when the disclosure is negative.

Sample size	For single cell RNA seq of CD45- cells, 9 5xFAD mice and 9 age-matched WTs were used. For GalC-enriched single cell RNA seq, the following mice were used: (6-8m)= 4AD, 4WT (10-11m)= 6AD, 5WT, (15m)= 3 AD, 3WT, (24m)= 4AD, 4WT. For mouse DOL quantification and plaque association from imaging, 4 5xFAD and 2 WT brain sections were used. For human DOL quantification from imaging, 8 postmortem AD patients and 8 non demented controls brain sections were used. sample sizes were chosen based on previous scRNA-seq data studie collected from mouse brain.
Data exclusions	In scRNA-seq analysis, cells with less than 350 UMIs and more than 20% of RNA mitochondrial content were removed from analysis as those can be considered as low-quality cells. Those criterion are widely used and have been established before performing the analysis.
Replication	Single-cell sorting and sequencing were performed multiple times as individual, independent experiments. Biological replicates (different mice) of the single cell RNAseq libraries were made for every experiment, and used as validations. Replications were successful and we report differences between WT and 5xFAD mice which are confirmed by all samples. For the time course data, we report differences between WT and 5xFAD mice that consistently increase or decrease across all time points. Biological replicates (different mice/patients) were used for the imaging analysis. Replications were successful and we report differences confirmed by all samples.
Randomization	In each experimental batch, animals were chosen randomly based on their age. However, we matched transgenic Alzheimer's model 5xFAD animals with WT non-transgenic litter-mate from the same mouse colony and age. No other experimental groups are relevant to this study.
Blinding	All basic scRNA-seq analysis steps (filtering, normalisation, clustering, cluster annotation…) were performed in a completely blinded manner. Microscopy image processing was done in a fully automated and un-supervised manner. For all other experimental procedures blinding is irrelevant (cell sorting was performed based on the same gate for all cells).

Reporting for specific materials, systems and methods

We require information from authors about some types of materials, experimental systems and methods used in many studies. Here, indicate whether each material, system or method listed is relevant to your study. If you are not sure if a list item applies to your research, read the appropriate section before selecting a response.

Materials & experimental systems

n/a	Involved in the study
☐	☒ Antibodies
☒	☐ Eukaryotic cell lines
☒	☐ Palaeontology and archaeology
☐	☒ Animals and other organisms
☐	☒ Human research participants
☒	☐ Clinical data
☒	☐ Dual use research of concern

Methods

n/a	Involved in the study
☒	☐ ChIP-seq
☐	☒ Flow cytometry
☒	☐ MRI-based neuroimaging

Antibodies

Antibodies used	For flow cytometry: anti-mouse CD45 APC (clone 30F-11, 17-0451-82, eBioscience or 103115, biolegend, 1:200),anti-mouse GalC

Antibodies used	(oligodendrocytes, FITC, clone mGalC, FCMAB312F, Milli-Mark, 1:10),anti-mouse Ly6A/E (endothelial, BV605, clone D7, 108133, Biolegend, 1:150). For mouse immunofluorescence: anti-mouse Olig2 (AB9610, Merck, 1:200), anti-mouse Serpina3n (AF4709, R&DSystems, 1:200), anti-human Aβ (BLG-803001, BioLegend, 1:200), donkey anti-rabbit cy2 (Jackson ImmunoResearch #711-225-152, 1:200), donkey anti-goat cy3 (Jackson ImmunoResearch #705-165-147, 1:200) and donkey anti-mouse cy5 (Jackson ImmunoResearch #715-175-151, 1:200). For human immunofluorescence: CC1 (ab16794, Abcam, 1:50), SERPINA3 (ab205198, Abcam, 1:100), donkey antirabbit cy5 (Jackson ImmunoResearch #711-175-152, 1:200) and donkey anti-mouse cy3 (Jackson ImmunoResearch #715-165-150, 1:200).
Validation	Full validations were done and staining with secondary antibody alone was used as a negative control, to rule out nonspecific staining. Primary antibody validation was performed by inspecting for non-specific staining (antibodies did not stain all the cells/ stained structures were not perfectly co-stained by all other antibodies used in the staining)and by difference in staining between conditions, if relevant. Sub-cellular localization was also inspected and compared to the reported staining pattern by the manufacturer.

Animals and other organisms

Policy information about studies involving animals; ARRIVE guidelines recommended for reporting animal research

Laboratory animals	In this study, the following mouse strains and ages were used: male and female heterozygous 5XFAD transgenic mice (Tg6799 strain on a C57/BL6-SJL strain background) and WT strain C57/BL6-SJL mice, at ages: 6-8m; n=4 5xFAD, 4 WT, 10-11m; n=6 5xFAD, 5 WT, 15m; n=3 5xFAD, 3 WT, 24m; n=4 5xFAD, 4 WT
Wild animals	The study did not include any wild animals.
Field-collected samples	The study did not include any samples collected at the field.
Ethics oversight	All experiments detailed herein complied with the regulations formulated by the Institutional Animal Care and Use Committee (IACUC) of the Weizmann Institute of Science.

Note that full information on the approval of the study protocol must also be provided in the manuscript.

Human research participants

Policy information about studies involving human research participants

Population characteristics	Post-mortem temporal cortical sections from 8 AD patients and 8 age matched non demented controls were obtained from Oxford Brain Bank. Sex was balanced between groups (5 males and 3 females per condition). ages ranged from 72-95 (mean: 84.3).
Recruitment	No donors were recruited. All participants gave prospective pre-mortem written consent for their brains to be banked and used for research.
Ethics oversight	All samples were approved by an Institutional Review Board (IRB) of Weizmann Institute of Science (ID: 1192-1).

Note that full information on the approval of the study protocol must also be provided in the manuscript.

Flow Cytometry

Plots

Confirm that:

☒ The axis labels state the marker and fluorochrome used (e.g. CD4-FITC).

☒ The axis scales are clearly visible. Include numbers along axes only for bottom left plot of group (a 'group' is an analysis of identical markers).

☒ All plots are contour plots with outliers or pseudocolor plots.

☒ A numerical value for number of cells or percentage (with statistics) is provided.

Methodology

Sample preparation	Mice were euthanized using an overdose of ketamine-xylazine, followed by transcardial perfusion with cold PBS and whole brains were harvested. Tissue was chopped to small pieces and subjected to 30 minutes of enzymatic digestion using papain (Worthington, LS003127) in 37oC, followed by manual trituration using 5ml pipette and filtering through a 70µm cell strainer. Cells were pelleted at 800g for 5 min in 4oC and then suspended in ovomucoid protease inhibitor (Worthington, LS003086) solution to stop papain activity. Cells were pelleted again in 600g, 5 min, 4oC, washed and myelin debris was removed by 30% percoll gradient (GE healthcare, 17-0891-01). Then, cells were pelleted and washed again and subjected to 20 min Fc block (1:200), following 30 min cell surface staining. Immediately before FACS reading, cells were washed, filtered through 70µm cell strainer, suspended in sorting buffer (PBS supplemented with 0.2mM EDTA pH8 and 0.5% BSA), and DAPI was added. Samples were kept on ice at all times except for enzymatic digestion.

Instrument	FACS-AriaIII (BD Biosciences, San Jose, CA)
Software	FACS DIVA software v8.0 (BD Biosciences, San Jose, CA)
Cell population abundance	Cells were single-cell sorted
Gating strategy	Dissociated brain cells were gated using FSC/SSC plot, dead cells were excluded by DAPI-positive staining, doublet exclusion was performed using FSC-A/FSC-H plot, autofluorescent cells were excluded using two empty autofluorescent channels (BUV737 and PE-cy7), oligodendrocytes were gated by CD45-GalC+ cells.

☒ Tick this box to confirm that a figure exemplifying the gating strategy is provided in the Supplementary Information.